Cu-EAB zeolite catalyst: A promising candidate with excellent SO2 poisoning resistance for NH3-SCR reaction

Cu-EAB zeolite catalyst: a promising candidate with excellent SO_2 poisoning resistance for NH_3-SCR reaction

Xiangqiong Jiang[1], Yu Sun[2], Rui Li[3], Dongdong Chen[4], Yuyan Yao[1], Zhifeng Zeng[1], Can Yang[1], Hongwei Chen[5], Hongzheng Chang[1], Yulong Shan[2], Carmine D'Agostino[6,7], Jiuxing Jiang[1*]

[1] MOE Key Laboratory of Bioinorganic and Synthetic Chemistry, School of Chemistry, IGCME, Sun Yat-sen University, Guangzhou 510006, China

[2] State Key Joint Laboratory of Environment Simulation and Pollution Control, Research Center for Eco-Environmental Sciences, Chinese Academy of Sciences, Beijing 100085, China

[3] State Key Laboratory of Green Chemical Engineering and Industrial Catalysis, SINOPEC Shanghai Research Institute of Petrochemical Technology Co., Ltd., Shanghai 201208, China

[4] School of Environmental and Chemical Engineering, Guangdong Provincial Key Laboratory of Environmental Health and Land Resource, Zhaoqing University, 526061 Zhaoqing, China

[5] College of Chemical Engineering and Technology, State Key Laboratory of Clean and Efficient Coal Utilization, Taiyuan University of Technology, Taiyuan 030024, China

[6] Department of Chemical Engineering, University of Manchester, Manchester, M13 9PL, UK

[7] Dipartimento di Ingegneria Civile, Chimica, Ambientale e dei Materiali (DICAM), Alma Mater Studiorum – Università di Bologna, Via Terracini, 28, 40131 Bologna, Italy

*corresponding authors: jiangjiux@mail.sysu.edu.cn (JX Jiang) Tel: +86-20-39339784

Abstract

In this work, we synthesized **Cu$_x$-EAB** catalysts with an **EAB** topology for the NH_3-SCR of NO_x and evaluated their resistance to SO_2 poisoning for the first time. The **Cu$_{2.53}$-EAB** catalyst showed superior NO_x conversion and selectivity for N_2, along with a notable tolerance to high space velocities and SO_2, outperforming the commercial **Cu$_{2.61}$-CHA** catalyst. This enhanced resistance was attributed to the Cu^{2+} species formation at the 2.53 wt% loading, which were mainly located in the double 6-rings and 8-rings of the **Cu$_{2.53}$-EAB** structure. The catalyst performance was stable even after SO_2 exposure and multiple NH_3-SCR cycles. Sulfation treatments at both 200 °C and 400 °C reduced the NO_x conversion rates of the **Cu$_{2.53}$-EAB** and **Cu$_{2.61}$-CHA** catalysts. Comparative characterizations before and after sulfation revealed that the NH_3-SCR activity of **Cu$_{2.53}$-EAB** was less affected by the sulfation treatment at 400 °C. The coverage of active sites by H_2SO_4 and $CuSO_4$ was identified as the primary cause of activity reduction for both catalysts after sulfation at 200 °C and 400 °C. A hybrid Langmuir-Hinshelwood (L-H) and Eley-Rideal (E-R) mechanism for the NH_3-SCR reaction over **Cu$_{2.53}$-EAB** was proposed, based on *in situ* DRIFTS analysis. The results show that the **Cu-EAB**

catalyst is a promising alternative for NH_3-SCR applications, offering improved SO_2 resistance and NO_x elimination capabilities.

Keywords: **EAB** zeolite, Cu content, NH_3-SCR, SO_2 resistance, X-ray Absorption Spectroscopy (XAS)

1. Introduction

A paramount technical hurdle in the wider adoption of diesel engines is the need for an efficient lean NO_x aftertreatment system, particularly under stringent emission standards [1]. Selective catalytic reduction with ammonia (NH_3-SCR) has emerged as one of the most promising technologies for NO_x elimination ($deNO_x$) [2-5]. Considerable efforts have focused on developing catalysts with excellent NO_x conversion efficiency, high N_2 selectivity, and strong resistance to sulfur dioxide (SO_2) poisoning [6-8]. The **Cu-CHA** catalyst is currently a widely used NH_3-SCR catalyst, renowned for its high activity and selectivity in NO_x reduction [9-13]. However, its performance is highly sensitive to sulfur poisoning, which is primarily caused by the catalyst exposure to SO_2, a component that can be present in engine exhaust under certain conditions. It's important to note that the prevalence of SO_2 in engine exhaust has been significantly reduced with the use of ultra-low sulfur diesel (ULSD), which restricts sulfur content to less than 15 ppm in the US and less than 10 ppm in Europe [14, 15]. However, the combustion of diesel fuel with such low sulfur content means that while SO_2 is not a prevalent component, it can still be generated and cause catalyst deactivation, especially in the presence of an upstream diesel oxidation catalyst (DOC) that can further oxidize SO_2 to SO_3 [16-18]. The generation of SO_3 on the catalyst is quite complex, as NO and NH_3 can promote the formation of SO_3. SO_3 reacts with NH_3 to form NH_4HSO_4 and $(NH_4)_2SO_4$, which deposit on the catalyst and downstream equipment causing corrosion [19-21]. This oxidation process can exacerbate the poisoning of the downstream SCR catalyst, highlighting the need for catalysts with improved sulfur resistance. In practical settings, even trace amounts of SO_2 can lead to the poisoning and deactivation of **CHA** zeolite catalysts. This sensitivity underscores the importance of understanding the interaction between SO_2 and **Cu-CHA** catalysts, as well as the development of strategies to mitigate sulfur poisoning [22, 23].

To address the concerns raised, we have explored alternative small-pore zeolites such as **LTA** [24], **AEI** [25], **AFX** [26], and **SFW** [27] with the aim of achieving enhanced $deNO_x$ performance and increased resistance to SO_2 poisoning. However, the synthesis of these zeolites often involves the use of environmentally detrimental fluoride ions or relies on costly raw materials, such as those required for **FAU** zeolites. Moreover, the synthesis processes for these

zeolites, which involve complex organic templates, can be both economically challenging and ecologically taxing.

In contrast, **EAB** zeolite presents a more sustainable and feasible alternative. As a small-pore zeolite with a hexagonal crystal system and an eight-membered ring channel structure measuring 0.37 × 0.51 nm, **EAB**'s framework consists of six-membered rings arranged in an ABBACC stacking pattern. This unique structure creates both a larger eab cage and a smaller gme cage, which are conducive to catalytic reactions. Importantly, the structural similarity of **EAB** to **CHA** zeolite suggests that it may offer comparable deNO_x efficacy in NH_3-SCR reactions, without the need for harmful ions or complex synthesis methods. The first silico-aluminite zeolite with an **EAB** topological structure was synthesized by Aiello and Barrer in 1970 using tetramethylammonium hydroxide (TMAOH) as a templating agent under rotational crystallization conditions [28]. Unlike the zeolites mentioned earlier, **EAB** zeolite does not necessitate the use of fluoride ions or costly raw materials, and its synthesis process is less complex, aligning with environmentally friendly practices [8]. Currently, **EAB** zeolite is still in the exploratory stages of synthesis and application, and its deployment in NH_3-SCR remains unreported [14, 15, 29, 30].

In this work, a systematic investigation was conducted on **Cu$_x$-EAB** catalysts with various Cu loadings, focusing on the impact of SO_2 on **Cu$_{2.53}$-EAB**. The results revealed that the **Cu$_{2.53}$-EAB** catalyst achieved the most favorable deNO_x performance, surpassing the commercial **Cu$_{2.61}$-CHA** catalyst with a Si/Al ratio of 5. After being exposed to 5% H_2O and SO_2 poisoning at both 200 °C and 400 °C for 50 h, the **Cu$_{2.53}$-EAB** catalyst maintained superior deNO_x efficiency compared to **Cu$_{2.61}$-CHA** catalyst, underscoring **EAB** zeolite's potential as a viable replacement for **CHA** zeolite in NH_3-SCR reactions. Furthermore, Time on Stream Behavior showed that the deNO_x performance of the **Cu$_{2.53}$-EAB** catalyst was superior to that of the **Cu$_{2.61}$-CHA** catalyst. The steady-state performance of NO_x was determined through sulfation, and kinetic analysis was used to quantitatively compare the changes in reactivity during the aging and sulfation processes. A series of characterization techniques, including XRD, NMR, NH_3-TPD, SO_2-TPD, EPR, H_2-TPR, XPS, *in situ* UV-vis, *in situ* DRIFTS, and XAS experiments, were employed to conduct a comprehensive and in-depth study of the effects of sulfur poisoning on both catalysts.

2. Experimental

2.1. Catalysts synthesis

In this work, **EAB** with a Si/Al molar ratio of 4.6 was prepared by using tetramethylammonium hydroxide (TMAOH) as organic structure directing agent (OSDA). The

obtained **EAB** were exchanged twice with 0.1 M CH_3COONH_4 (97 wt.%, Aladdin) solution and stirred at 80 °C for 2 h to acquire **NH_4-EAB**. **NH_4-EAB** was then exchanged with 0.01, 0.02, 0.03 and 0.05 $Cu(NO_3)_2 \cdot 3H_2O$ (99 wt.%, Aladdin) solution and stirred at 80 °C for 24 h. The **Cu_x-EAB** catalysts were washed with deionized water and dried at 120 °C overnight. The **Cu_x-EAB** catalysts (*x* presents the mass fraction of Cu, *x* = 1.06 wt.%, 2.06 wt.%, 2.53 wt.% and 3.06 wt.%) were obtained after calcination under the program of increasing the temperature to 290 °C and maintained for 2 h and then further raising to 450 °C for 6 h.

For comparison, SSZ-13 was also synthesized through a hydrothermal process using 1-adamantyltrimethylammonium hydroxide (TMAdaOH, Kente Catalysts) as the OSDA. The molar composition of reaction synthesis gel has a similar ratio with SSZ-13 that is Si: 0.1 Al: 0.11 TMAdaOH: 0.7 NaOH: 20 H_2O. The obtained SSZ-13 samples were exchanged twice with 0.1 M CH_3COONH_4 (97 wt.%, Aladdin) solution and stirred at 80 °C for 2 h to acquire NH_4-SSZ-13. The preparation procedures for Cu-SSZ-13 was identical to that of the **Cu-EAB** catalysts.

2.2. Catalysts characterization

The element contents, including the Si/Al ratio and Cu loading, were determined using a Vario El elemental analyzer and IRIS (HR) inductively coupled plasma-atomic emission spectrometry (ICP-OES). The crystal structures of the catalysts was investigated by X-ray powder diffraction (XRD) using a Smart Lab instrument. The surface areas and pore size distributions were analyzed through N_2 adsorption-desorption measurements using a Micromeritics ASAP 2020 Plus. Catalyst morphologies were observed with a scanning electron microscope (SEM, Hitachi SU8010, Japan). The properties of the Cu species were examined by X-ray photoelectron spectroscopy (XPS, Thermo Fisher Scientific) and temperature programmed reduction of H_2 (H_2-TPR) using an MFTP-3060 chemisorption analyzer. Electron paramagnetic resonance (EPR) experiments were conducted using a Bruker A300 instrument, while UV-vis diffuse reflection spectroscopy (UV-vis-DRS) was performed on a Shimadzu UV 3600 instrument. The acidic properties of the catalysts were investigated by temperature programmed desorption of ammonia (NH_3-TPD) with an MFTP-3060 chemisorption analyzer. The ^{27}Al solid-state nuclear magnetic resonance (^{27}Al NMR) spectra were recorded using a Bruker AVANCE III 500 to explore the dealumination of the catalysts. The reaction mechanism was investigated by *in situ* diffuse reflectance infrared Fourier transform spectroscopy (*in situ* DRIFTS) using a Thermo Scientific Nicolet 6700 instrument. Additional experimental details are provided in the **Supplementary Information**.

2.3. Activity tests and kinetic measurements

The deNO$_x$ activity and kinetic experiments of all the catalysts were conducted in a fixed bed with a quartz flow reactor. For the experiments, the catalyst was pelletized and sieved to obtain particles in the size range of 40-60 mesh. We loaded 100 mg of the catalyst into a quartz tube with an inner diameter of 4 mm for the NH_3-SCR experiments. The feed mixture gases were composed of 500 ppm NO, 500 ppm NH_3, 5% O_2, and N_2 balance. Meanwhile, the total flow rate was 200 mL min^{-1} for the GHSV of 100, 000 h^{-1}. The outlet gas contents (NO, NO_2, N_2O, and NH_3) were analyzed by Thermo Scientific Nicolet Antaris IGS equipped with a TCD detector.

$$NO_x \text{ conversion} = \frac{[NO]_{in}-[NO]_{out}-[NO_2]_{out}-2[N_2O]_{out}}{[NO]_{in}} \times 100\% \quad (1)$$

$$N_2 \text{ selectivity} = \frac{[NO]_{in}+[NH_3]_{in}-[NO]_{out}-[NH_3]_{out}-[NO_2]_{out}-2[N_2O]_{out}}{[NO]_{in}+[NH_3]_{in}-[NO]_{out}-[NH_3]_{out}} \times 100\% \quad (2)$$

The activation energy of Cu$_x$-EAB catalysts was calculated using the Arrhenius equation, as follows:

$$\ln K = -\frac{Ea}{RT} + \ln A \quad (3)$$

Where K, R, Ea, T, and A are used to denote the chemical reaction rate constant, molar gas constant, apparent activation energy, reaction temperature, and pre-exponential factor, respectively.

3. Results

3.1. Analysis of NH_3-SCR catalytic performance

The NO$_x$ conversion of all catalysts was illustrated in **Fig.1A**. The **Cu$_{1.06}$-EAB** exhibited the lowest NO$_x$ conversion between 150 °C and 200 °C, achieving over 90% conversion at 250 °C. As the Cu content increased, a notable improvement in NO$_x$ conversion was observed within the temperature range of 150 to 200 °C. The **Cu$_{2.53}$-EAB** demonstrated the highest deNO$_x$ performance, maintaining a NO$_x$ conversion rate exceeding 90% from 200 to 450 °C across the broader temperature range of 200 to 550 °C. **Fig.1B** presented the N_2 selectivity of the **Cu$_x$-EAB** catalysts, all of which maintained over 98% N_2 selectivity throughout the entire temperature range.

The influence of various gas hourly space velocities (GHSVs) (100,000, 200,000, and 400,000 h^{-1}) on the deNO$_x$ performance of NH_3-SCR was investigated, with the **Cu$_{2.53}$-EAB** catalyst as the focus (**Fig. S1**). While the NH_3-SCR performances at GHSVs of 100,000 and 200,000 h^{-1} were found to be comparable within the experimental error, increasing the GHSV to 400,000 h^{-1} resulted in a noticeable decrease in NO$_x$ conversion across the temperature range of 150 to 550 °C. This reduction in conversion at higher GHSV is likely due to non-ideal plug

flow behavior and potential bypassing effects in the reactor, rather than a change in the intrinsic catalyst activity. Based on the observations, the optimal GHSV for **$Cu_{2.53}$-EAB** was determined to be 200,000 h^{-1}.

Kinetic parameters of **Cu_x-EAB** catalysts were calculated at NO_x conversions below 20%, as depicted in **Fig. 1C** and outlined in **Table 2**. The apparent activation energy (E_a) values, derived from Arrhenius plots, were found to be 107.9, 86.9, 55.2, 55.1, and 66.7 kJ mol^{-1} for **$Cu_{1.06}$-EAB, $Cu_{2.06}$-EAB, $Cu_{2.53}$-EAB, $Cu_{3.06}$-EAB** and **$Cu_{2.53}$-EAB(SO_2)**, respectively. A significant decrease in E_a was observed with increasing amounts of Cu ion exchange, which can be attributed to several factors influencing the catalyst's active sites and the reaction mechanism. As the Cu content increased, there was likely an enhancement in the dispersion of Cu species within the zeolite framework, leading to the formation of more active sites available for the NH_3-SCR reaction. This increase in active site density lowered the E_a by providing more opportunities for reactant molecules to interact and form products, thus facilitating the reaction at lower energies. Moreover, the nature of the active sites may also have changed with increased Cu ion exchange. The introduction of more Cu ions could have led to the formation of Cu species that had a lower energy requirement for the reaction to proceed, thereby reducing the E_a. This change in active site nature could have involved the creation of more accessible or more reactive Cu sites that lowered the energy barrier for the reaction. The decrease in E_a with increasing Cu ion exchange suggested that the catalyst's active sites and reaction mechanism were sensitive to the Cu content, and an optimal amount of Cu (2.53%) could be determined to achieve the most favorable balance between activity and energy requirements for the NH_3-SCR reaction. Notably, the E_a values for **$Cu_{2.53}$-EAB** and **$Cu_{2.53}$-EAB(SO_2)** were similar, indicating that the presence of SO_2 had a minimal impact on the activation energy of the **$Cu_{2.53}$-EAB** catalyst. This similarity in E_a values highlighted the robustness of the **$Cu_{2.53}$-EAB** catalyst, as it maintained its catalytic activity even under the influence of SO_2. The comparable E_a values for **$Cu_{2.53}$-EAB** and **$Cu_{3.06}$-EAB** suggested that both catalysts exhibited similar catalytic activity at lower temperatures, aligning with their performance under the optimal GHSV conditions. The **$Cu_{2.53}$-EAB** catalyst stood out for its low activation energy and its ability to retain high catalytic activity in the presence of SO_2, demonstrating its potential as a reliable catalyst for NH_3-SCR applications where sulfur resistance was a critical factor.

Residual sulphur dioxide (SO_2) in exhaust gases significantly impacts the NH_3-SCR system. The SO_2 tolerance of **$Cu_{2.53}$-EAB** and **$Cu_{2.61}$-CHA** was evaluated under a GHSV of 200,000 h^{-1} (**Fig. 1D**). SO_2 poisoning experiments were conducted on **$Cu_{2.53}$-EAB** and **$Cu_{2.61}$-CHA** in the presence of 5% water at 400 °C for 50 h. The NO_x conversion of **$Cu_{2.53}$-EAB(SO_2)** slightly

decreased across all temperatures, whereas that of **Cu$_{2.61}$-CHA(SO$_2$)** showed a substantial decline, illustrating the robust anti-SO_2 poisoning capability of **Cu$_{2.53}$-EAB**. To validate the impact of low-temperature SO_2 poisoning on catalyst performance, both catalysts were subjected to sulfation at 200 °C in the presence of water (**Fig. S2**). The results indicated that sulfation at 200 °C led to a certain degree of decrease in NO_x conversion rates for both catalysts. However, compared to **Cu$_{2.53}$-EAB**, the SCR activity of **Cu$_{2.61}$-CHA** was more significantly affected by sulfation at both 200 °C and 400 °C. This suggests that **Cu$_{2.53}$-EAB** exhibits a higher tolerance to SO_2 poisoning across the tested temperature range. The reason for the greater impact on **Cu$_{2.61}$-CHA** at these temperatures can be attributed to differences in the catalysts' structures and active site distributions. **Cu$_{2.53}$-EAB**, with its unique **EAB** topology, may provide a more stable environment for the active Cu species, reducing their susceptibility to SO_2-induced deactivation. Additionally, the **EAB** structure might offer a more robust framework that resists the formation of inactive sulfate species, which are known to block active sites and decrease catalyst activity.

Additionally, side-product analysis for both **Cu$_{2.53}$-EAB** and **Cu$_{2.61}$-CHA** revealed very low levels of NO_2 (< 5 ppm) and N_2O (< 5 ppm), indicating high selectivity of NO to N_2 conversion (**Fig. S3**). For the SO_2-poisoned catalysts, **Cu$_{2.53}$-EAB(SO$_2$)** showed no significant changes in NO_2 and N_2O concentrations, whereas **Cu$_{2.61}$-CHA(SO$_2$)** experienced notable fluctuations, with maximum concentrations of NO_2 and N_2O reaching 12 and 24 ppm at 200 °C, respectively. These results demonstrate that the **Cu$_{2.53}$-EAB** catalyst not only exhibits excellent activity, N_2 selectivity, and resistance to high space velocity, but also outstanding anti-SO_2 poisoning ability.

In our comparative evaluation of the SO_2 poisoning resistance of **Cu$_{2.53}$-EAB** and **Cu$_{2.61}$-CHA** catalysts during the NH_3-SCR reaction, we conducted experiments at a temperature of 400 °C and a GHSV of 200,000 h^{-1}, introducing 100 ppm of SO_2 and 5% H_2O into the reaction mixture. As depicted in **Fig. S4**, the feed contained 500 ppm NH_3, 500 ppm NO, 5 vol.% O_2, 5 vol.% H_2O, 100 ppm SO_2, and was balanced with N_2 at a GHSV of 200,000 h^{-1}. Prior to the introduction of SO_2, both catalysts achieved a stable 98% NO_x conversion at 400 °C over a period of 2 h. Upon the introduction of 100 ppm SO_2, the NO_x conversion rate of the **Cu$_{2.61}$-CHA** catalyst gradually decreased from 98% to 31% over an 8 h period, and only recovered to 65% of its original efficiency when SO_2 was removed, with a continued downward trend in NO_x conversion stability. In contrast, the **Cu$_{2.53}$-EAB** catalyst exhibited a more robust resistance to SO_2 poisoning; its NO_x conversion rate declined from 99% to 82% over a 3 h period. Although the NO_x conversion rate gradually decreased with extended testing, it stabilized at approximately 45% after 17 h. Upon removal of SO_2, the NO_x conversion

efficiency recovered to 79% and remained stable. These results demonstrated that the **$Cu_{2.53}$-EAB** catalyst possessed superior SO_2 resistance compared to the **$Cu_{2.61}$-CHA** catalyst under the tested conditions at 400 °C.

Fig. S5, where the feed contained 500 ppm NH_3, 500 ppm NO, 5 vol.% O_2, 5 vol.% H_2O, and was balanced with N_2 at a GHSV of 200,000 h^{-1}, depicted the activity stability of **$Cu_{2.53}$-EAB(SO_2)** and **$Cu_{2.61}$-CHA(SO_2)** catalysts over time at temperatures of 200 °C, 300 °C, and 400 °C for 10 h. The result illustrated that both catalysts exhibited stable performance across the 200 °C and 300 °C. However, the **$Cu_{2.53}$-EAB(SO_2)** catalyst maintained a higher level of stability compared to the **$Cu_{2.61}$-CHA(SO_2)** catalyst. Throughout the test duration, the **$Cu_{2.53}$-EAB(SO_2)** catalyst's activity remained relatively constant, even after exposure to SO_2. This indicated that the **$Cu_{2.53}$-EAB** catalyst possessed an inherent resistance to SO_2 poisoning, a trait that was highly desirable for catalysts used in environments where SO_2 may be present. The stability of the **$Cu_{2.53}$-EAB(SO_2)** catalyst at all tested temperatures underscored its potential for real-world applications, where catalysts were often subjected to fluctuating conditions and potential exposure to sulfur compounds. The consistent performance of the **$Cu_{2.53}$-EAB(SO_2)** catalyst indicated that it could withstand the challenges posed by SO_2, making it a robust candidate for use in NH_3-SCR systems.

3.2. Synthesis of the zeolite

The synthesis of **EAB** zeolite is a complex process that is highly dependent on the selection and proportion of raw materials, as well as the precise control of crystallization conditions. As delineated in **Table 1**, initial attempts to synthesize the **EAB** zeolite using tetraethyl orthosilicate (TEOS) as a silicon source and sodium aluminate ($NaAlO_2$) as an aluminum source at temperatures of 80, 100, and 150 °C failed to produce a pure **EAB** phase. These temperatures were insufficient to induce the necessary structural transformations towards the **EAB** topology. A pivotal breakthrough was achieved by replacing TEOS with fumed silica (SiO_2), which is known for its high purity and reactivity. This change, coupled with extended crystallization durations of 7 days at 80 °C and 4 days at 100 °C, facilitated the formation of a pure **EAB** zeolite phase. At a higher crystallization temperature of 150 °C for a duration of 2 days, the product predominantly displayed a SOD structure, indicating the sensitivity of zeolite formation to temperature and time. Through meticulous experimentation, the optimal molar ratios of the reactants were determined to be crucial for the synthesis. The dosage of $NaAlO_2$ was refined to a range of 1.1 to 1.5, and NaOH to a range of 6.0 to 8.0. These ratios were found to be instrumental in achieving the desired zeolite structure. Consequently, fumed silica was selected as the silicon source for the synthesis of **EAB** zeolite, based on its effectiveness in promoting

the formation of the desired crystal phase. The final optimized molar ratio for the synthesis of EAB zeolite was established as 10Si: 1.5Al: 5.0OSDA: 8.0NaOH: 80 H_2O. This ratio ensured the formation of **EAB** zeolite with a well-defined structure, which is essential for its application in NH_3-SCR reactions.

3.3. Analysis of the zeolite and catalysts framework

Scanning Electron Microscope (SEM) images of all samples (**Fig. S6**) displayed a cubic morphology characteristic of **EAB** zeolite, suggesting that the introduction of Cu did not alter the original morphology of **EAB** zeolite [28]. Post-sulfur treatment, the catalysts maintained a high degree of crystallinity, preserving integrity of the **EAB** structure. Powder X-ray Diffraction (PXRD) patterns, as depicted in **Fig. 2A**, exhibited typical diffraction peaks consistent with the **EAB** and **CHA** structures, with no detectable peaks for CuO_x species. This confirmed that the introduction of Cu did not perturb the structural integrity of the **EAB** zeolite framework. Notably, the crystallinity of both **$Cu_{2.53}$-EAB(SO_2)** and **$Cu_{2.61}$-CHA(SO_2)** catalysts decreased post-SO_2 poisoning, yet **$Cu_{2.53}$-EAB(SO_2)** maintained the highest relative crystallinity among the two catalysts, underscoring its enhanced resistance to sulfur-induced degradation. The ^{27}Al MAS NMR spectra of the zeolites and catalysts, presented in **Fig. 2B**, identified peaks at 59, 55, 30, and -1 ppm, corresponding to tetrahedrally coordinated framework Al (AlO_4), distorted tetrahedra, pentacoordinate Al (AlO_5), and extra-framework octahedral Al (AlO_6), respectively [31, 32]. The increased intensity of the peak at 58 ppm across all fresh catalysts suggested that the introduction of Cu enhanced the structural integrity of the zeolite framework. The disappearance of a broad signal around 30 ppm, attributed to pentacoordinate framework Al, indicated a reduction in such species upon Cu ion exchange. Post-SO_2 treatment, the proportion of octahedral Al in **$Cu_{2.53}$-EAB(SO_2)** increased compared to **$Cu_{2.53}$-EAB**, suggesting some dealumination occurred during the sulfation process. In contrast, the spectrum of **$Cu_{2.61}$-CHA(SO_2)** exhibited significant broadening, indicating a more pronounced distortion of the **CHA** framework structure. Despite some degradation, **$Cu_{2.53}$-EAB** retained its **EAB** structure post-sulfuric acid treatment, demonstrating that the impact of SO_2 poisoning on the framework structure of **EAB** zeolite was less severe than that on **CHA** zeolite. These findings underscored the resilience of **$Cu_{2.53}$-EAB** against sulfur poisoning, maintaining its structural integrity and crystallinity better than **$Cu_{2.61}$-CHA**, which was critical for sustaining catalytic performance in NH_3-SCR applications where sulfur resistance was paramount.

The N_2 adsorption-desorption isotherms and pore size distributions (**Fig. S4**) confirmed the typical microporous structure inherent to **EAB** zeolite. The Brunauer–Emmett–Teller (BET) surface areas and pore volumes of all the samples were summarized in **Fig. 2(E and F)** and

Table 2, demonstrated the following values: 196 m^2 g^{-1} and 0.20 cm^3 g^{-1} (**H-EAB**), 186 m^2 g^{-1} and 0.20 cm^3 g^{-1} (**$Cu_{1.06}$-EAB**), 184 m^2 g^{-1} and 0.20 cm^3 g^{-1} (**$Cu_{2.06}$-EAB**), 176 m^2 g^{-1} and 0.20 cm^3 g^{-1} (**$Cu_{2.53}$-EAB**), 164 m^2 g^{-1} and 0.20 cm^3 g^{-1} (**$Cu_{2.53}$-EAB(SO_2)**), 69 m^2 g^{-1} and 0.09 cm^3 g^{-1} (**$Cu_{3.06}$-EAB**), respectively. In the case of **$Cu_{2.61}$-CHA**, SO_2 poisoning resulted in a notable reduction in BET surface areas and pore volumes from 572 m^2 g^{-1} and 0.20 cm^3 g^{-1} to 488 m^2 g^{-1} and 0.18 cm^3 g^{-1}, respectively. This indicated that SO_2 poisoning disrupted the zeolite framework of the **$Cu_{2.61}$-CHA** catalyst, compromising its structural integrity. In comparison, the BET surface area and pore volume of **$Cu_{2.53}$-EAB** and **$Cu_{2.53}$-EAB(SO_2)** showed only a slight decrease compared to **H-EAB**, whereas those of **$Cu_{3.06}$-EAB** exhibited a significant reduction. This suggests that SO_2 poisoning had a minimal impact on the specific surface area and pore volume of **$Cu_{2.53}$-EAB**, highlighting its superior resistance to SO_2 poisoning compared to **$Cu_{2.61}$-CHA**. The preservation of the BET surface area and pore volume in **$Cu_{2.53}$-EAB** after SO_2 exposure indicated the robustness of its structure, which is crucial for maintaining catalytic activity under conditions where SO_2 is present. In contrast, the substantial decrease in BET surface area and pore volume for **$Cu_{3.06}$-EAB** underscores the sensitivity of this catalyst to SO_2 poisoning, leading to a loss in structural integrity and catalytic performance.

To further confirm the Si/Al ratios of the prepared zeolites, ^{29}Si MAS NMR spectra of **$Cu_{2.53}$-EAB**, **$Cu_{2.53}$-EAB(SO_2)**, **$Cu_{2.61}$-CHA** and **$Cu_{2.61}$-CHA(SO_2)** were analyzed (**Fig. S7**). The peaks at S4 (-111 ppm) were attributed to the Si(0Al) structure, while the signals at S3 (-105 ppm), S2 (-100 ppm) and S1 (-93 to -96 ppm) corresponded to Si(0Al), Si(1Al), Si(2Al) and Si(3Al) structures, respectively [31, 33]. The percentages of different Si coordination structures in the fresh and poisoned catalysts were calculated by deconvolution and are presented in **Table S1.** The results indicated that the proportion of the Si(0Al) structure increased following sulfation, rising from 38.3% in **$Cu_{2.53}$-EAB** to 46.0% in **$Cu_{2.53}$-EAB(SO_2)**, and from 35.3% in **$Cu_{2.61}$-CHA** to 49.2% in **$Cu_{2.61}$-CHA(SO_2)**. The trend suggests that SO_2 poisoning induces a significant restructuring of the zeolite framework, primarily through dealumination. During this process, aluminum atoms are preferentially removed from the framework, leaving an increased number of silicon atoms unassociated with aluminum (Si(0Al)), thereby raising the Si/Al ratio. The structural transformation was more pronounced in **$Cu_{2.61}$-CHA(SO_2)**, which exhibited a higher increase in the Si(0Al) structure ratio compared to its fresh counterpart. This indicates that the sulfation process selectively targets aluminum atoms, leading to greater framework modifications in the **CHA**-based catalyst. The Si/Al derived from NMR values for **$Cu_{2.53}$-EAB**, **$Cu_{2.53}$-EAB(SO_2)**, **$Cu_{2.61}$-CHA**, and **$Cu_{2.61}$-CHA(SO_2)** were 4.3, 4.9, 4.5, and 5.7, respectively. Interestingly, these NMR-derived Si/Al ratios were lower than those obtained via ICP

measurements, which was an unexpected outcome. This discrepancy likely arises because NMR predominantly detects surface species, while ICP provides an average composition of the entire catalyst. As a result, the observed difference highlights the complementary nature of these techniques for characterizing catalyst structures.

3.4. Analysis of the surface acidity

NH_3 temperature-programmed desorption (NH_3-TPD) experiments were conducted to assess changes in surface acidity following the introduction of Cu species and subsequent sulfation (**Fig. 3**). The NH_3 desorption curve was deconvoluted into three distinct peaks (**Fig. 3A**), corresponding to NH_3 adsorbed on weak Brønsted acid sites (terminal −OH group), Lewis acid sites (Cu sites), and strong Brønsted acid sites (Si−OH−Al sites) [34-36]. It is noteworthy that at a Cu concentration of 2.53 wt%, the **$Cu_{2.53}$-EAB** catalyst exhibited the highest density of Lewis acid sites. Moreover, compared to **H-EAB**, the strong acid sites in **$Cu_{2.53}$-EAB** were significantly increased. This suggested that the introduction of 2.53 wt% Cu effectively enhances the formation of both Lewis and strong Brønsted acid sites, thereby facilitating the adsorption of NH_3 and potentially boosting the catalyst's overall activity. However, increasing the Cu concentration to 3.06% resulted in the disappearance of strong Brønsted acid sites, a decrease in new strong Lewis acid sites, and an increase in weak Brønsted acid sites. Post sulfur poisoning, the Lewis acid sites in **$Cu_{2.53}$-EAB** were reduced, while the weak Brønsted acid sites increased, indicating a loss of some active Cu species due to SO_2 exposure (**Fig. 3B**). The total acidity of all catalysts was calculated and displayed in **Table 2**, with values of 3.33, 3.89, 3.92, 4.01, 3.02, 1.77, 4.01 and 3.12 $mmol \cdot g^{-1}$ for **H-EAB**, **$Cu_{1.06}$-EAB**, **$Cu_{2.06}$-EAB**, **$Cu_{2.53}$-EAB**, **$Cu_{2.53}$-EAB(SO_2)**, **$Cu_{3.06}$-EAB**, **$Cu_{2.61}$-CHA** and **$Cu_{2.61}$-CHA(SO_2)**, respectively. The results showed that **$Cu_{2.53}$-EAB** had the highest NH_3 adsorption. Following high-temperature SO_2 treatment, the NH_3 adsorption capacity of **$Cu_{2.53}$-EAB (SO_2)** was slightly reduced, which was consistent with EPR results. In contrast, **$Cu_{3.06}$-EAB** exhibited the lowest NH_3 adsorption, suggesting that excessive Cu loading led to a reduction or loss of strong, medium, and weak acid sites, adversely impacting NH_3-SCR performance. The introduction of 2.53 wt% Cu effectively created new Lewis acid sites, enhancing NH_3 absorption and demonstrating relative resilience against high temperature SO_2 toxicity.

To further probe the the nature and quantity of acid sites, *in situ* DRIFTS analysis of NH_3 adsorption and desorption on **$Cu_{2.53}$-EAB** were conducted (**Fig. S8)**. After NH_3 adsorption for 60 min and subsequent purging with pure N_2 for another 60 min at 100 °C, several peaks were identified, corresponding to NH_3 adsorbed on Si-(OH)-Al sites (3650 and 3588 cm^{-1}), Brønsted acid sites (1772, 1469 and 1190 cm^{-1}), Lewis acid sites (1606 and 1130 cm^{-1}) and T-O-T bonds

by exchanged Cu ions (950 and 900 cm^{-1}) [37, 38]. As the temperature increased, the intensity of NH_3 peaks gradually decreased. Notably, at 500 °C, the peak at 1469 cm^{-1} showed significant resilience, indicative of NH_3 adsorption on strong Brønsted acid sites. These results confirm that the NH_3 desorption peak at 400 °C was indicative of NH_3 adsorption at newly formed Lewis acid sites, such as Cu^{2+} species. The NH_3 adsorption-desorption experiment validated that the acid sites were preserved in **$Cu_{2.53}$-EAB**, consistent with NH_3-TPD results.

3.5. Analysis of the sulfur species

To elucidate the sulfated species formed during sulfation, SO_2-TPD experiments were conducted. As depicted in **Fig. 4**, **$Cu_{2.53}$-EAB** and **$Cu_{2.61}$-CHA** were subjected to SO_2 poisoning under conditions of 5% H_2O/air and 100 ppm SO_2 at 200 and 400 °C. To mitigate the influence of the zeolite framework, **H-EAB** and **H-CHA** were treated with SO_2 at 400 °C, designated as **H-EAB(SO_2)-400** and **H-CHA(SO_2)-400**, respectively. The A peak near 200-300 °C is attributed to the decomposition of the weakly adsorbed molecular SO_2, while peaks B around 400-500 °C and C around 500-800 °C are assigned to H_2SO_4 and $CuSO_4$ species for all catalysts [39, 40]. Compared to **H-EAB(SO_2)-400**, **H-CHA(SO_2)-400** not only exhibited $CuSO_4$ species but also H_2SO_4 species. It was understood that the presence of sulfuric acid had exacerbated the collapse of the zeolite framework, indicating that the framework of **EAB** zeolite was more sulfur-resistant than that of **CHA** zeolite. The strong acidity of H_2SO_4 had corroded the zeolite's silicon-aluminum framework, leading to the breakage of Si-O-Si and Al-O-Al bonds. Additionally, H_2SO_4 had reacted with metal cations in the zeolite to form sulfates that may have accumulated within the zeolite pores, causing blockage and structural deformation. The presence of water molecules had further exacerbated these effects, especially under high temperature and humidity conditions. Furthermore, H_2SO_4 had transformed active sites within the zeolite into sulfates, reducing the catalyst's activity. The stability of the zeolite structure had been compromised, particularly under hydrothermal conditions where Si-O(H)-Al bonds were susceptible to breaking, leading to dealumination and structural degradation.

Concurrently, **$Cu_{2.53}$-EAB** and **$Cu_{2.61}$-CHA** were treated with SO_2 at 200 and 400 °C, denoted as **$Cu_{2.53}$-EAB(SO_2)-200**, **$Cu_{2.53}$-EAB(SO_2)-400**, **$Cu_{2.61}$-CHA(SO_2)-200**, and **$Cu_{2.61}$-CHA(SO_2)-400**. The SO_2-TPD results indicated that after sulfation at 200 °C, **$Cu_{2.53}$-EAB(SO_2)-200** contained less H_2SO_4 than **$Cu_{2.61}$-CHA(SO_2)-200**. Post sulfation at 400 °C, H_2SO_4 species in **$Cu_{2.53}$-EAB(SO_2)-400** were notably diminished, whereas **$Cu_{2.61}$-CHA(SO_2)-400** contained significantly less H_2SO_4 than **$Cu_{2.61}$-CHA(SO_2)-200**. The relationship between H_2SO_4 and NO_x conversion suggests that the presence of H_2SO_4 was one of the primary causes of catalytic activity decline. Additionally, the presence of H_2SO_4 in the catalysts damaged the

framework, indicating that sulfation led to more severe degradation of the **CHA** framework compared to **EAB** zeolite, consistent with XRD and NMR results. In the case of **Cu2.61-CHA** catalysts, sulfuric acid may have also promoted the aggregation of Cu^{2+} ions into CuO_x clusters that were larger than the zeolite pores, which could eventually have led to the collapse of the zeolite framework. Notably, compared to 200 °C, **Cu2.53-EAB(SO2)-400** exhibited a significantly reduced sorptive capacity for SO_2 after sulfation at 400 °C, indicating that the formation of H_2SO_4 species in **Cu2.53-EAB** catalysts was greatly suppressed, demonstrating the superior sulfur resistance of **Cu2.53-EAB**. Concurrently, $CuSO_4$ was also a cause of catalytic activity decline at low temperatures. For the samples sulfated with sulfuric acid, **Cu2.53-EAB(SO2)-200** retained the most $CuSO_4$ species. With increasing SO_2 treatment temperature, the size of peak C decreased for both catalysts, indicating that temperature increases altered the nature of Cu sites, reducing their affinity for sulfur.

The integrated SO_2 desorption amounts for all samples were also provided. The SO_2 desorption quantities for the catalysts **H-EAB**, **H-CHA**, **Cu2.53-EAB(SO2)-200**, **Cu2.53-EAB(SO2)-400**, **Cu2.61-CHA(SO2)-200**, and **Cu2.61-CHA(SO2)-400** were measured as 0.08, 0.11, 1.04, 1.08, 0.42, and 0.52 mmol/g, respectively. These values provided a quantitative assessment of the sulfur retention capacity of each catalyst after exposure to SO_2. The desorption data indicated a clear trend in sulfur uptake among the catalysts. **H-EAB** and **H-CHA**, which were the parent zeolites without Cu, exhibited the lowest SO_2 desorption quantities, suggesting that the presence of Cu in the **Cu2.53-EAB** and **Cu2.61-CHA** catalysts significantly influences their sulfur adsorption behavior. Specifically, **Cu2.53-EAB(SO2)-200** and **Cu2.53-EAB(SO2)-400** showed substantially higher SO_2 desorption quantities compared to their parent **H-EAB**, highlighting the role of Cu in enhancing sulfur adsorption. Comparing the two Cu-containing catalysts, **Cu2.53-EAB(SO2)-200** and **Cu2.53-EAB(SO2)-400**, with their **Cu-CHA** counterparts, **Cu2.61-CHA(SO2)-200** and **Cu2.61-CHA(SO2)-400**, it was evident that the **EAB**-based catalysts had lower SO_2 desorption quantities. This suggested that the **EAB** framework, even with Cu incorporation, had a lower affinity for sulfur compared to the **CHA** framework. The lower desorption quantities for **Cu2.53-EAB(SO2)-200** and **Cu2.53-EAB(SO2)-400** also suggested that these catalysts were less prone to sulfur poisoning, which was a desirable characteristic for catalysts operating in environments with potential SO_2 exposure. Furthermore, the decrease in SO_2 desorption quantity from **Cu2.53-EAB(SO2)-200** to **Cu2.53-EAB(SO2)-400** after sulfation at 400 °C indicates that the higher temperature treatment reduced the sulfur retention capacity of the catalyst. This reduction could be due to the decomposition of sulfur species at elevated temperatures, leading to a decrease in the amount of sulfur retained

by the catalyst. The lower desorption quantities for the **$Cu_{2.53}$-EAB** catalysts compared to **$Cu_{2.61}$-CHA** catalysts underscore the superior sulfur resistance of **$Cu_{2.53}$-EAB**, which is a critical factor for their stability and performance in NH_3-SCR applications.

3.6. Analysis of the active Cu species

Electron Paramagnetic Resonance (EPR) experiments were conducted to investigate the coordination environment of isolated Cu^{2+} species across the **Cu-EAB** catalysts with varying copper concentrations **(Fig. 5A and C)** [41]. A distinct peak, characterized by g// = 2.40 and A// = 130 G, was observed for all catalysts, indicative of isolated Cu^{2+} species [42]. The signal intensity increased with the concentration of Cu ions, with **$Cu_{2.53}$-EAB** showing the most pronounced signal, except for **$Cu_{3.06}$-EAB**, where a higher prevalence of CuO_x species might be inferred, suggesting a shift in Cu species distribution. Following SO_2 treatment, the peak area of **$Cu_{2.53}$-EAB(SO_2)** was slightly reduced compared to that of **$Cu_{2.53}$-EAB**, indicating that the quantity of Cu^{2+} was not significantly diminished after sulfur exposure. This suggested that **$Cu_{2.53}$-EAB** maintains a substantial amount of its active Cu^{2+} species even after SO_2 treatment, which was a desirable trait for catalysts operating in environments containing SO_2. In comparison, **$Cu_{2.61}$-CHA(SO_2)** exhibited a more pronounced decrease in peak intensity after SO_2 treatment, indicating a greater loss of active Cu^{2+} species. This suggested that **$Cu_{2.61}$-CHA** was more susceptible to SO_2 poisoning, leading to a reduction in the number of available active sites and a consequent decrease in catalytic performance. The observed slight weakening of the fine structure for both catalysts after SO_2 treatment can be attributed to the interaction of Cu^{2+} species with the zeolite framework being disrupted by sulfur exposure. This disruption was more pronounced in **$Cu_{2.61}$-CHA**, leading to a more significant loss of active sites. Furthermore, the retention of a larger amount of Cu^{2+} species in **$Cu_{2.53}$-EAB(SO_2)** compared to **$Cu_{2.61}$-CHA(SO_2)** after SO_2 exposure underscores the superior SO_2 resistance of **$Cu_{2.53}$-EAB**. This finding was consistent with the results obtained from XRD, NH_3-TPD, and ^{27}Al NMR results, which collectively indicated that **$Cu_{2.53}$-EAB** not only maintains its structural integrity but also preserves its active site population better than **$Cu_{2.61}$-CHA** under similar conditions of SO_2 exposure. These comprehensive characterizations provided a clear picture of the impact of SO_2 on the active copper species and the structural stability of the two catalysts, highlighting the resilience of **$Cu_{2.53}$-EAB** in the presence of SO_2.

Hydrogen Temperature-Programmed Reduction (H_2-TPR) experiments were employed to elucidate the redox behavior of active Cu^{2+} species across the **Cu-EAB** catalysts with varying copper concentrations, before and after SO_2 treatment (**Fig. 5B and D**). Employing fixed peak positions for $Cu(OH)^+$-Z, Cu^{2+}-2Z, CuO_x and $Cu(AlO_2)_2$ species at 240~255, 305, 400, and

520 °C respectively, we analyzed the H_2-TPR profiles comprehensively, with detailed results presented in Table S1 [27, 43, 44]. **$Cu_{2.53}$-EAB** exhibited the highest total amount of active Cu^{2+} species, highlighting its rich active site population. Post-SO_2 treatment, **$Cu_{2.53}$-EAB(SO_2)** showed no detectable CuO_x species, in contrast to **$Cu_{3.06}$-EAB**, which noted a 21% occurrence of CuO_x species (**Table S2**). This indicated that while additional Cu promotes the formation of $Cu(OH)^+$-Z and Cu^{2+}-2Z species, excessive Cu can lead to the generation of CuO_x species, sensitive to SO_2 poisoning. For the **$Cu_{2.53}$-EAB(SO_2)** catalyst, the peak in the range of 240~255 °C decreased, while the peaks at 400 and 520 °C increased, suggesting that a portion of the reduced $Cu(OH)^+$-Z sites transformed into more stable Cu^{2+}-2Z sites. In comparison, the **$Cu_{2.61}$-CHA(SO_2)** catalyst showed a near disappearance of the 240~255 °C peak, a weakening of the 400 °C peak, and an increase in the 520 °C peak. This new feature can be attributed to the transformation of $Cu(OH)^+$-Z and Cu^{2+}-2Z into highly disordered $Cu(AlO_2)_2$ species due to SO_2 treatment. Notably, both **$Cu_{2.53}$-EAB(SO_2)** and **$Cu_{2.61}$-CHA(SO_2)** catalysts did not exhibit reduction peaks around 305 °C, indicating that SO_2 treatment did not lead to an increase in CuO_x clusters. These findings corroborate the EPR results, indicating that SO_2 has a minimal impact on the deactivation of Cu species in the **$Cu_{2.53}$-EAB** catalyst. The preservation of active Cu^{2+} species in **$Cu_{2.53}$-EAB** after SO_2 exposure, as evidenced by both H_2-TPR and EPR, further validates its superior sulfur resistance compared to **$Cu_{2.61}$-CHA**. These comprehensive characterizations underscore the resilience of **$Cu_{2.53}$-EAB** against SO_2-induced deactivation, maintaining its active site population and redox properties, which is crucial for its catalytic performance in NH_3-SCR applications.

In situ Diffuse Reflectance Infrared Fourier Transform Spectroscopy (*in situ* DRIFTS) was utilized to examine the impact of SO_2 treatment on the Cu^{2+} species within **$Cu_{2.53}$-EAB** and **$Cu_{2.61}$-CHA** catalysts. The spectra, post-NH_3 adsorption saturation, were depicted in **Fig. 5E**. The negative peaks at 950 and 900 cm^{-1}, corresponding to zeolite T-O-T vibrations perturbed by $Cu(OH)^+$-Z (8-ring) and Cu^{2+}-2Z (6-ring) respectively, were indicative of the active Cu species' presence. For **$Cu_{2.53}$-EAB**, the area ratio of Cu^{2+}-2Z species was higher than that of $Cu(OH)^+$-Z, signifying the dominance of Cu^{2+}-2Z as the active species. Following SO_2 treatment, the signals for both Cu^{2+}-2Z and $Cu(OH)^+$-Z in **$Cu_{2.53}$-EAB(SO_2)** diminished, with a more significant reduction observed for $Cu(OH)^+$-Z. This aligns with EPR results, indicating a shift in the Cu species' distribution. In contrast, **$Cu_{2.61}$-CHA** exhibited a marked decrease in $Cu(OH)^+$-Z species' content from 17.6% to 6.0% post-SO_2 treatment, corroborating H_2-TPR findings. Notably, SO_2 treatment induced a redshift in the two negative peaks for **$Cu_{2.61}$-CHA**, suggesting a change in the copper species' interaction with the zeolite framework. This redshift

is attributed to the perturbation of the T-O-T vibrations due to the formation of less ordered or more dispersed Cu species, indicative of a structural change in the catalyst framework. **$Cu_{2.53}$-EAB**, however, showed no significant peak shift post-SO_2 treatment, indicating the retention of its active copper species' structure and stability. Compared to **$Cu_{2.61}$-CHA(SO_2)**, **$Cu_{2.53}$-EAB(SO_2)** preserved a greater amount of $Cu(OH)^+$-Z species, which explains its maintained high catalytic activity. This preservation of active Cu species, as evidenced by the unchanged peak positions and the higher retention of $Cu(OH)^+$-Z species, underscores **$Cu_{2.53}$-EAB's** superior sulfur resistance. The resistance of **$Cu_{2.53}$-EAB** to sulfur poisoning is further supported by *in situ* DRIFTS results, which showed that **$Cu_{2.53}$-EAB** retained the most active Cu species post-SO_2 treatment.

To enhance the detection of Cu species and mitigate interference from water, the samples were subjected to high-temperature dry air pre-treatment. *In situ* DRUVS spectra for all catalysts were presented in **Fig. S9**. The spectral regions at 200-450 nm and 450-750 nm were attributed to charge transitions from the lattice oxygen of the zeolite to Cu^{2+}/Cu^+ ions and d-d transitions in distorted octahedral Cu^{2+} within the zeolite framework, respectively. These assignments are consistent with the literature on Cu species in zeolites, which aids in the interpretation of our spectra [45]. The peak intensity associated with CuO_x species increased with increasing Cu content, which was in agreement with H_2-TPR results, indicating a correlation between Cu content and the presence of CuO_x species. The *in situ* DRUVS spectra revealed a slight increase in CuO_x accumulation in **$Cu_{2.53}$-EAB(SO_2)** after high-temperature sulfur treatment compared to **$Cu_{2.53}$-EAB**, suggesting that sulfation had a limited impact on the catalyst. The minimal change observed in **$Cu_{2.53}$-EAB(SO_2)** suggested that this catalyst retains its active Cu species and structural integrity even under sulfur-rich conditions.

X-ray Photoelectron Spectroscopy (XPS) analysis was conducted to elucidate the changes in copper species within **$Cu_{2.53}$-EAB** and **$Cu_{2.61}$-CHA** catalysts before and after SO_2 treatment. The Cu *2p* XPS spectra **(Fig. 5F)** exhibited peaks at 933.1 and 934.0 eV, corresponding to Cu^+ and Cu^{2+} states, respectively [46-48]. After deconvolution, the integral area fractions of these species were quantified and presented in **Table S3**. The relative amounts of Cu^{2+} species across the catalysts were as follows: 0.16 for **$Cu_{1.06}$-EAB**, 0.25 for **$Cu_{2.06}$-EAB**, 0.40 for **$Cu_{2.53}$-EAB**, and 0.27 for **$Cu_{3.06}$-EAB**. This indicates that with increasing Cu amounts, the proportion of Cu^{2+} species increased while that of Cu^+ diminished. Notably, **$Cu_{2.53}$-EAB** contained the highest relative amount of Cu^{2+}, which is key for catalytic activity in NH_3-SCR. After SO_2 treatment, the Cu^{2+} content in **$Cu_{2.53}$-EAB** decreased from 0.40 to 0.32, while in **$Cu_{2.61}$-CHA**, it dropped from 0.28 to 0.17. Comparing the fresh catalysts, **$Cu_{2.53}$-EAB(SO_2)** had a higher

Cu^{2+} species content than **$Cu_{2.61}$-CHA(SO_2)**. This significant decrease in Cu^{2+} species in **$Cu_{2.61}$-CHA** post-SO_2 treatment suggests that SO_2 has a more pronounced effect on **$Cu_{2.61}$-CHA**, leading to a faster deactivation of Cu^{2+} species compared to **$Cu_{2.53}$-EAB**. The higher Cu^{+} content in both catalysts compared to Cu^{2+} can be attributed to the reducing nature of the NH_3-SCR environment, which favors the reduction of Cu^{2+} to Cu^{+}. However, **$Cu_{2.53}$-EAB's** higher initial Cu^{2+} content and its relative stability post-SO_2 treatment suggest a more robust resistance to sulfur poisoning, which is crucial for maintaining catalytic activity.

This resistance is further supported by H_2-TPR results, which showed that **$Cu_{2.53}$-EAB** retained the most active Cu species post-SO_2 treatment. The preservation of active Cu species, as evidenced by XPS, EPR, and H_2-TPR, underscores **$Cu_{2.53}$-EAB's** superior sulfur resistance compared to **$Cu_{2.61}$-CHA**. These findings are consistent with DRIFTS results, which indicated minimal changes in the active site structure of **$Cu_{2.53}$-EAB** post-SO_2 treatment, further validating its potential as a robust catalyst for NH_3-SCR applications where sulfur resistance is essential.

3.7. Analysis of reaction mechanisms

NH_3 and NO + O_2 adsorption. *In situ* Diffuse Reflectance Infrared Fourier Transform Spectroscopy (*in situ* DRIFTS) was employed to scrutinize the adsorption behavior of fresh and SO_2-poisoned **$Cu_{2.53}$-EAB** and **$Cu_{2.61}$-CHA** catalysts towards NH_3 and NO_x, shedding light on their active site dynamics (**Fig. 6**). After NH_3 adsorption for 60 min, the DRIFTS spectra of two fresh catalysts revealed several peaks, indicating a robust adsorption capacity for NH_3 (**Fig. 6A**). Notably, **$Cu_{2.53}$-EAB** exhibited a more pronounced adsorption capacity compared to **$Cu_{2.61}$-CHA**, suggesting a higher density of accessible active sites. SO_2 poisoning led to the disappearance or reduction of two fresh catalysts peaks at 3650 and 3588 cm^{-1}, corresponding to Si-OH-Al sites, due to the consumption of hydroxyl groups [37, 38]. Peaks at 1772 and 1469 cm^{-1} are attributed to NH_3 adsorbed on Brønsted acid sites, while peaks at 1623, 1255, and 1164 cm^{-1} are associated with NH_3 adsorbed on Lewis acid sites [49-55]. Significantly, the peaks at 956 and 900 cm^{-1} are indicative of NH_3 adsorption on $Cu(OH)^{+}$-Z and Cu^{2+}-2Z species, respectively. The intense peaks at 900 cm^{-1} for both **$Cu_{2.53}$-EAB** and **$Cu_{2.61}$-CHA** catalysts suggest that Cu^{2+}-2Z species in the double 6-ring structure dominate in these catalysts. The adsorption of NH_3 revealed that the acid sites of both poisoned catalysts were compromised (**Fig. 6B**), consistent with NH_3-TPD results. Specifically, the disappearance of the peak at 956 cm^{-1} for **$Cu_{2.61}$-CHA(SO_2)** indicates the loss of $Cu(OH)^{+}$-Z species, aligning with H_2-TPR findings [37, 38]. Following NO and O_2 adsorption experiments (**Fig. 6B**), SO_2 poisoning resulted in a slight weakening of peaks at 1735 (N_2O_4 species), 1635 (gas-phase NO_2), and 1508

cm^{-1} (bidentate species) for **$Cu_{2.53}$-EAB(SO_2)**, indicating a diminished capacity to adsorb NO_x post-poisoning [56, 57]. For **$Cu_{2.61}$-CHA**, peaks at 1762 (N_2O_4 species) and 1635 cm^{-1} (gas-phase NO_2) disappeared post-poisoning, signifying a more severe impact on NO_x adsorption. The higher Cu^+ content compared to Cu^{2+} in both catalysts can be attributed to the reducing environment of the NH_3-SCR process, which favors the reduction of Cu^{2+} to Cu^+. However, **$Cu_{2.53}$-EAB** retains a higher proportion of Cu^{2+} species post-SO_2 treatment, suggesting its superior resistance to sulfur poisoning. In conclusion, **$Cu_{2.53}$-EAB** demonstrated a superior ability to retain active copper species and acid sites, and also maintain its adsorption capacity for both NH_3 and NO_x after SO_2 poisoning, highlighting its enhanced sulfur resistance compared to **$Cu_{2.61}$-CHA**. These findings are corroborated by EPR, H_2-TPR, and DRIFTS results, which collectively underscore the robustness of **$Cu_{2.53}$-EAB** in NH_3-SCR applications.

Sequential NH_3 and NO + O_2 adsorption. To deepen the understanding of the NH_3-SCR mechanism over **$Cu_{2.53}$-EAB**, a series of *in situ* DRIFTS experiments were conducted (**Fig. 6**). The initial step involved investigating the reaction of pre-adsorbed NH_3 with gaseous NO and O_2 over the catalyst (**Fig. 6C**). Initially, the catalyst had been exposed to NH_3 for 60 min, achieving saturation of the Brønsted and Lewis acid site. Notable negative peaks were observed at 3573 and 3666 cm^{-1}, indicative of the depletion of surface silanol and Brønsted acid sites (Al-OH groups) due to NH_3 adsorption. Peaks at 1163, 1471, and 1745 cm^{-1}, indicative of stretching and bending vibrations of the N-H bond in NH_4^+ at Brønsted acid sites, had been observed [58, 59]. The emergence of near 1255 and 1608 cm^{-1} were attributed to NH_3 species on Lewis acid sites (Cu ions) [37, 38]. Following the completion of N_2 purging for 60 min, the introduction of NO and O_2 commenced. The peak at 1608 cm^{-1} initially decreased and subsequently increased, overlapping with a nitrate peak, signifying that Lewis acid sites were interacting with both Cu^{2+} ions and NH_3. Thus, the 60 min peak near 1608 cm^{-1} was associated with nitrate species coordinated by Cu^{2+}. Concurrently, the peak at 1563 cm^{-1} also belonged to nitrate species, becoming the dominant species after 60 min of NO and O_2 injection [60]. The negative peaks at 952 and 896 cm^{-1} were attributed to T-O-T perturbations of $Cu(OH)^+$-Z and Cu^{2+}-2Z, respectively [61]. The introduction of NO and O_2 was found to lead to the formation of nitrate intermediates (1608 and 1563 cm^{-1}), crucial for the Langmuir-Hinshelwood (L-H) mechanism. Moreover, NH_3 bound to the Lewis acid sites was continually consumed with the ongoing introduction of NO and O_2, leading to a significant reduction in all NH_3 peak intensities. Notably, NH_3 associated with the Lewis acid site (1608 cm^{-1}) was consumed more rapidly than that bound to the Brønsted acid site (1471 cm^{-1}) within the first 10 min, suggesting greater instability at the Lewis sites. All NH_3 adsorption peaks had disappeared within 30 min,

concurrent with nitrate production, indicating that the Eley-Rideal (E-R) mechanism also played a role. These findings suggested that both the L-H and E-R mechanisms coexisted in the NH_3-SCR process of **$Cu_{2.53}$-EAB**.

Sequential NO + O_2 and NH_3 adsorption. *In situ* DRIFTS spectra of NH_3 interacting with pre-adsorbed NO + O_2 over **$Cu_{2.53}$-EAB** were also shown in **Fig. 6D**. The **$Cu_{2.53}$-EAB** catalyst had initially been exposed to NO and O_2 for 60 min until saturation was reached. Subsequently, NH_3 was introduced after N_2 purging for a further 60 min. Peaks between 1606 and 1570 cm^{-1} were ascribed to Cu-NO_3^-, had shown a decrease in intensity following the introduction of NH_3, indicating the consumption of nitrate species by ammonia and reinforcing the presence of the Langmuir-Hinshelwood mechanism [52, 62]. Within approximately 4 min of NH_3 introduction, adsorption peaks appeared at 3650 and 3588 cm^{-1} for NH_3 on Si-OH-Al sites, at 1772, 1469, and 1255 cm^{-1} for Brønsted acid sites, and at 1606 and 1164 cm^{-1} for Lewis acid sites, along with stretching vibrations from NH_3 on Cu sites (946 and 896 cm^{-1}) [37, 38]. These peaks remained stable as NH_3 was introduced for about 30 min. By 10 min, the peak at 1570 cm^{-1} disappeared, indicating that the absorbed nitrate species had been consumed. This process had demonstrated that the L-H mechanism in **$Cu_{2.53}$-EAB** proceeded at a faster rate than the E-R mechanism, with nitrates serving as critical intermediates in the L-H mechanism. As previously stated, the L-H mechanism played a pivotal role in the NH_3-SCR process of the **$Cu_{2.53}$-EAB**, with nitrate acting as a crucial intermediate in the L-H mechanism. The redox cycle of the NH_3-SCR process on **$Cu_{2.53}$-EAB**, involving the reduction of Cu^{2+} by NO and NH_3 to form N_2 and H_2O and the oxidative reactivation of O_2 and NO by Cu^+ to form nitrates, was identified as the rate-determining step. Additionally, the NH_3 and NO_x adsorption results of *in situ* DRIFTS analysis proved that the adsorption of NO_x was weaker compared with NH_3 adsorption for **$Cu_{2.53}$-EAB** (**Fig. S10**). These interactions suggested that the catalysts predominantly operated via the E-R and L-H mechanisms both contributing at 200 °C, based on the differential adsorption behaviors of pre-adsorbed species.

3.8. Analysis of XANES and extended EXAFS

The X-ray absorption spectroscopy was employed to decipher the oxidation states and coordination environments of Cu in the **$Cu_{2.53}$-EAB, $Cu_{2.53}$-EAB(SO_2), $Cu_{2.61}$-CHA, $Cu_{2.61}$-CHA(SO_2)** and **$Cu_{2.53}$-EAB-used** (after five NH_3-SCR cycle experiments). **Fig. 7** presented the K-edge XANES spectra of Cu foil, Cu_2O, CuO, and $CuSO_4$, along with the spectra of all the catalysts under investigation. A noteworthy initial peak at approximately 8982 eV was identified, characteristic of a hydrated, non-dipole Cu^+ species that can undergo a quadrupole

1s to 4p transition [63, 64]. The pre-edge peak at around 8978.0 eV is indicative of a dipole-forbidden but quadrupole-allowed 1s to 3d transition for hydrated Cu^{2+} ions. Furthermore, the pre-edge peaks at 8981.9 and 8985.4 eV are assignable to Cu_2O and CuO_x species, respectively, suggesting that CuO_x species were either absent or present in negligible quantities in the **$Cu_{2.53}$-EAB**, **$Cu_{2.53}$-EAB(SO_2)**, **$Cu_{2.61}$-CHA** and **$Cu_{2.53}$-EAB-used** catalysts [27]. However, it was observed that the **$Cu_{2.61}$-CHA(SO_2)** catalyst contained a portion of CuO_x species, which is indicative of the formation of inactivated CuO_x species due to SO_2 poisoning. This difference in the Cu species distribution highlighted the impact of SO_2 on the catalyst's structure and activity. The inclusion of $CuSO_4$ in the analysis was instrumental in validating the presence of isolated Cu^{2+} ions, which were essential active sites for the NH_3-SCR reaction. The peak observed at 8997.5 eV for the **$Cu_{2.53}$-EAB**, **$Cu_{2.53}$-EAB(SO_2)**, and **$Cu_{2.53}$-EAB-used** catalysts was attributed to Cu^{2+} species existing in a high coordination environment. This observation confirmed that Cu^{2+} species were the predominant form in these catalysts, highlighting the robustness of the **$Cu_{2.53}$-EAB** catalysts even after exposure to SO_2 and multiple reaction cycles.

The post-edge spectra and fitting results for **$Cu_{2.53}$-EAB, $Cu_{2.53}$-EAB(SO_2), $Cu_{2.61}$-CHA, $Cu_{2.61}$-CHA(SO_2)** and **$Cu_{2.53}$-EAB-used** catalysts were shown in **Fig. 8** and **Table S4**. EXAFS spectra confirmed that the average coordination number and bond length of Cu in **$Cu_{2.53}$-EAB** and **$Cu_{2.61}$-CHA** catalysts were similar (4 and 1.93 Å, respectively) (**Table S4**). These results confirmed the similarity in the coordination environment of Cu in both fresh catalysts. The first shell peak intensity at 1.5 Å for **$Cu_{2.53}$-EAB-used** and **$Cu_{2.53}$-EAB(SO_2)** catalysts remained consistent, indicating that NH_3-SCR cycles and sulfidation did not lead to significant loss of OH ligands in the first coordination sphere of Cu sites in **$Cu_{2.53}$-EAB** catalysts [63-65]. For **$Cu_{2.61}$-CHA**, sulfation results in a coordination number lower than 4, and the peak intensity at 1.5 Å for **$Cu_{2.61}$-CHA(SO_2)** was reduced, primarily due to the transformation of Cu^{2+} into CuO_x during the sulfation process. It was noteworthy that the bond length remained unchanged for both sulfided catalysts, indicating that sulfation had minimal impact on the bond length. The results suggested that sulfation had a lesser impact on the coordination environment of **$Cu_{2.53}$-EAB** compared to **$Cu_{2.61}$-CHA** catalysts.

4. Discussion

In this work, we compared the NH_3-SCR performance of **Cu-EAB** and **Cu-CHA** zeolites, focusing on their resistance to SO_2 poisoning. The **EAB** and **CHA** zeolites, both members of the three-dimensional (3D) 8-ring channel small-pore zeotypes, are uniquely comprised of 6-ring units. While their structures differ primarily in the packing sequence of these 6-rings, with **EAB** adopting an ABBACC arrangement and **CHA** featuring a simpler AABBCC pattern, both

zeolites were expected to demonstrate comparable $DeNO_x$ performance in the NH_3-SCR reaction. Our results indicated that the **$Cu_{2.53}$-EAB** catalyst outperformed the commercial **$Cu_{2.61}$-CHA** catalyst in terms of NO_x conversion and selectivity for N_2, particularly under conditions of high space velocities and SO_2 exposure. The **$Cu_{2.53}$-EAB** catalyst maintained its performance stability even after SO_2 exposure and multiple NH_3-SCR cycles, a testament to its superior resistance to SO_2 poisoning. This enhanced resistance was attributed to the optimized formation of Cu^{2+} species at the 2.53 wt% loading, which were primarily located in the double 6-rings and 8-rings of the **$Cu_{2.53}$-EAB** structure, a feature that contributed to its higher tolerance to SO_2 compared to **$Cu_{2.61}$-CHA**. Sulfation treatments at 200 °C and 400 °C were applied to both catalysts, and it was observed that the NO_x conversion rates decreased for both. However, comparative characterizations before and after sulfation revealed that the NH_3-SCR activity of **$Cu_{2.53}$-EAB** was less affected by the sulfation treatment at 400 °C compared to **$Cu_{2.61}$-CHA**. The coverage of active sites by H_2SO_4 and $CuSO_4$ was identified as the primary cause of activity reduction for both catalysts after sulfation at 200 °C and 400 °C, with **$Cu_{2.53}$-EAB** showing a greater resistance to such coverage. A hybrid Langmuir-Hinshelwood (L-H) and Eley-Rideal (E-R) mechanism for the NH_3-SCR reaction over **$Cu_{2.53}$-EAB** was proposed, based on *in situ* DRIFTS analysis. This mechanism coexistence suggests a more complex and potentially more robust catalytic process in **$Cu_{2.53}$-EAB** compared to **$Cu_{2.61}$-CHA**, which may contribute to its superior SO_2 resistance and NO_x elimination capabilities. In conclusion, the **$Cu_{2.53}$-EAB** zeolite, with its unique structure and Cu^{2+} species distribution, demonstrated a superior ability to resist SO_2 poisoning and maintain catalytic activity, making it a promising alternative for NH_3-SCR applications where SO_2 resistance is crucial.

5. Conclusion

In summary, the **$Cu_{2.53}$-EAB** zeolite catalyst, synthesized with a Si/Al ratio of 4.6 using TMAOH as the OSDA, demonstrated superior $deNO_x$ performance and resistance to SO_2 poisoning compared to the commercial **$Cu_{2.61}$-CHA** catalyst. The **$Cu_{2.53}$-EAB** catalyst maintained its $deNO_x$ efficacy under pre- and post-SO_2 poisoning conditions, which was a significant advancement over the **$Cu_{2.61}$-CHA** catalysts that are prone to deactivation under similar conditions. The comprehensive characterization of zeolite and **Cu_x-EAB** catalysts, including their microporous structure, redox capacity, acid sites, location and amount of active Cu species, and the low-temperature reaction mechanism, revealed that the exceptional NH_3-SCR catalytic activity of the **Cu_x-EAB** catalysts is linked to the location and concentration of the active Cu^{2+} species. The **$Cu_{2.53}$-EAB** catalyst's active sites were predominantly Cu^{2+} species located in the double 6-ring (d6r) and 8-ring (8r), exhibiting similar coordination environments,

each with an average coordination number of 4. The introduction of a moderate amount of Cu (2.53 wt%) facilitated the formation of new Lewis acid sites, enhancing NO_x reduction. *In situ* DRIFTS revealed that the **$Cu_{2.53}$-EAB** exhibited a mixed L-H and E-R mechanism, with NH_3 dominating the surface adsorption competition compared to NO_x. SO_2 poisoning and five NH_3-SCR cycles experiments showed that the coordination environment of **$Cu_{2.53}$-EAB** remained essentially unaffected, highlighting its superior sulfur resistance. The **$Cu_{2.53}$-EAB** catalyst's superior resistance to SO_2 poisoning was further supported by EPR, H_2-TPR, and XPS results, which showed that it retained a substantial amount of its active Cu^{2+} species even after SO_2 treatment. This was in contrast to **$Cu_{2.61}$-CHA**, which exhibited a greater loss of active Cu^{2+} species after SO_2 exposure. The preservation of active Cu species in **$Cu_{2.53}$-EAB**, as evidenced by these characterizations, underscores its superior sulfur resistance compared to **$Cu_{2.61}$-CHA**. These findings are consistent with DRIFTS results, which indicated minimal changes in the active site structure of **$Cu_{2.53}$-EAB** post-SO_2 treatment, further validating its potential as a robust catalyst for NH_3-SCR applications where sulfur resistance is essential. This work provides a guideline to design other novel zeolite catalysts with high anti-SO_2 ability that can be applied for NH_3-SCR reaction.

Declaration of Competing Interest

The authors declare that they have no known competing financial interests or personal relationships that could have appeared to influence the work reported in this paper.

Acknowledgments

This work was supported by the National Natural Science Foundation of China (No. 22372200, 22306155) and Guangdong Provincial Science and Technology (2021B1212050005).

References

[1] P. Granger, V.I. Parvulescu, 2011. Catalytic NO_x abatement systems for mobile sources: From three-way to lean burn after-treatment technologies. Chem Rev. 111, 3155-3207.

[2] J. Du, J. Wang, Y. Shan, S. Han, W. Shan, H. He, 2024. Promoted NH_3-SCR activity and hydrothermal stability of Cu-SSZ-50 catalyst synthesized by one-pot method. Chin Chem Lett. 35, 108781.

[3] F. Wang, P. Wang, J. Zhang, D. Peng, M. Wei, D. Zhang, 2024. Deactivation mechanisms and anti-deactivation strategies of molecular sieve catalysts for NO_x reduction. Chin Chem Lett. 35, 108800.

[4] C. Chang, Z. Yan, C. Zhang, Y. Zhang, M. Jiang, L. Ruan, M. Xiao, Y. Yu, H. He, 2024. Design of Ca-type todorokite catalysts with highly active for the selective reduction of NO_x by NH_3 at low temperatures. J Environ Sci. 138, 697-708.

[5] Y. Zhu, W. Shan, Z. Lian, J. Liu, Y. Zhang, H. He, 2024. Effects of impregnation sequence on the NH_3-SCR activity and hydrothermal stability of a Ce-Nb/SnO_2 catalyst. J Environ Sci. 138, 450-457.

[6] Y.J. Kim, J.K. Lee, K.M. Min, S.B. Hong, I.-S. Nam, B.K. Cho, 2014. Hydrothermal stability of CuSSZ13 for reducing NO_x by NH_3. J Catal. 311, 447-457.

[7] Y. Shan, J. Du, Y. Yu, W. Shan, X. Shi, H. He, 2020. Precise control of post-treatment significantly increases hydrothermal stability of in-situ synthesized cu-zeolites for NH_3-SCR reaction. Appl Catal B-Environ. 266, 118655.

[8] A. Guo, H. Liu, Y. Li, Y. Luo, D. Ye, J. Jiang, P. Chen, 2023. Recent progress in novel zeolite catalysts for selective catalytic reduction of nitrogen oxides. Catal Today. 422, 114212.

[9] Z. Zhao, R. Yu, C. Shi, H. Gies, F.-S. Xiao, D. De Vos, T. Yokoi, X. Bao, U. Kolb, R. McGuire, A.-N. Parvulescu, S. Maurer, U. Müller, W. Zhang, 2019. Rare-earth ion exchanged Cu-SSZ-13 zeolite from organotemplate-free synthesis with enhanced hydrothermal stability in NH_3-SCR of NO_x. Catal Sci Technol. 9, 241-251.

[10] Z. Zhao, R. Yu, R. Zhao, C. Shi, H. Gies, F.-S. Xiao, D. De Vos, T. Yokoi, X. Bao, U. Kolb, M. Feyen, R. McGuire, S. Maurer, A. Moini, U. Müller, W. Zhang, 2017. Cu-exchanged Al-rich SSZ-13 zeolite from organotemplate-free synthesis as NH_3-SCR catalyst: Effects of Na^+ ions on the activity and hydrothermal stability. Appl Catal B-Environ. 217, 421-428.

[11] W. Eijima, G. Shibata, N. Shibayama, Y. Kobashi, H. Ogawa, K.-i. Shimizu, 2020. Kinetic modeling of steady-state NH_3-SCR over a monolithic Cu-CHA catalyst. Catal Today 352, 237-242.

[12] J. Liang, Y. Mi, G. Song, H. Peng, Y. Li, R. Yan, W. Liu, Z. Wang, P. Wu, F. Liu, 2020. Environmental benign synthesis of Nano-SSZ-13 via FAU trans-crystallization: Enhanced NH_3-SCR performance on Cu-SSZ-13 with nano-size effect. J Hazard Mater. 398, 122986.

[13] H. Tian, Y. Ping, Y. Zhang, Z. Zhang, L. Sun, P. Liu, J. Zhu, X. Yang, 2021. Atomic layer deposition of silica to improve the high-temperature hydrothermal stability of Cu-SSZ-13 for NH_3 SCR of NO_x. J Hazard Mater. 416, 126194.

[14] P.S. Hammershoi, Y. Jangjou, W.S. Epling, A.D. Jensen, T.V.W. Janssens, Reversible and irreversible deactivation of Cu-CHA NH_3-SCRcatalysts by SO_2 and SO_3, Appl. Catal. B: Environ, 226 (2018) 38-45.

[15] C. Wang, J. Wang, J. Wang, T. Yu, M. Shen, W. Wang, W. Li, The effect of sulfate species

on the activity of NH_3-SCR over Cu/SAPO-34, Appl. Catal. B: Environ, 204 (2017) 239-249.
[16] A.Y. Molokova, E. Borfecchia, A. Martini, I.A. Pankin, C. Atzori, O. Mathon, S. Bordiga, F. Wen, P.N.R. Vennestrøm, G. Berlier, T.V.W. Janssens, K.A. Lomachenko, SO_2 Poisoning of Cu-CHA deNO_x Catalyst: The Most Vulnerable Cu Species Identified by X-ray Absorption Spectroscopy, JACS Au, 2 (2022) 787-792.
[17] J. Lu, Z. Zhou, H. Zhang, Z. Yang, Influenced factors study and evaluation for SO_2/SO_3 conversion rate in SCR process, Fuel, 245 (2019) 528-533.
[18] L. Huang, Y. Zeng, Y. Gao, H. Wang, Y. Zong, Z. Chang, S. Zhang, P. Han, Y. Yu, Promotional effect of phosphorus addition on improving the SO_2 resistance of V_2O_5-MoO_3/TiO_2 catalyst for NH_3-SCR of NO, J. Phys. Chem. Solids, 163 (2022) 110566.
[19] H. Xiao, Y. Chen, C. Qi, Y. Ru, Effect of Na poisoning catalyst (V_2O_5–WO_3/TiO_2) on denitration process and SO_3 formation, Appl. Surf. Sci., 433 (2018) 341-348.
[20] M. Qing, S. Su, L. Wang, L. Liu, Z. Sun, M.E. Mostafa, K. Xu, S. Hu, Y. Wang, J. Xiang, Effects of H_2O and CO_2 on the catalytic oxidation property of V/W/Ti catalysts for SO_3 generation, Fuel, 237 (2019) 545-554.
[21] M. Qing, S. Su, L. Wang, L. Liu, K. Xu, L. He, X. Jun, S. Hu, Y. Wang, J. Xiang, Getting insight into the oxidation of SO_2 to SO_3 over V_2O_5-WO_3/TiO_2 catalysts: Reaction mechanism and effects of NO and NH_3, Chem. Eng. J., 361 (2019) 1215-1224.
[22] Q. Huang, L. Song, H. He, W. Qiu, Y. Su, 2016. Effects of SO_2 treatment of commercial catalysts on selective catalytic reduction of NO_x by NH_3. Chem Res Chin Univ. 32, 414-417.
[23] Q. Lin, C. Lin, J. Liu, S. Liu, H. Xu, Y. Chen, Y. Dan, 2020. Optimization of hybrid crystal with SAPO-5/34 on hydrothermal stability for deNO_x reaction by NH_3. Chem Res Chin Univ. 36, 1249-1254.
[24] T. Ryu, N.H. Ahn, S. Seo, J. Cho, H. Kim, D. Jo, G.T. Park, P.S. Kim, C.S. Kim, E.L. Bruce, P.A. Wright, I.-S. Nam, S.B. Hong, 2017. Fully copper-exchanged high-silica LTA zeolites as unrivaled hydrothermally stable NH_3-SCR catalysts. Angew Chem Int Ed. 56, 3256-3260.
[25] X. Ye, J.E. Schmidt, R.P. Wang, I.K. van Ravenhorst, R. Oord, T. Chen, F. de Groot, F. Meirer, B.M. Weckhuysen, 2020. Deactivation of Cu-exchanged automotive-emission NH_3-SCR catalysts elucidated with nanoscale resolution using scanning transmission X-ray microscopy. Angew Chem Int Ed. 59, 15610-15617.
[26] G. Shibata, W. Eijima, R. Koiwai, K.-i. Shimizu, Y. Nakasaka, Y. Kobashi, Y. Kubota, M. Ogura, J. Kusaka, 2019. NH_3-SCR by monolithic Cu-ZSM-5 and Cu-AFX catalysts: Kinetic modeling and engine bench tests. Catal Today 332, 59-63.

[27] R. Li, Y. Zhu, Z. Zhang, C. Zhang, G. Fu, X. Yi, Q. Huang, F. Yang, W. Liang, A. Zheng, J. Jiang, 2021. Remarkable performance of selective catalytic reduction of NO_x by ammonia over copper-exchanged SSZ-52 catalysts. Appl Catal B-Environ. 283, 119641.

[28] T. Hagio, J.H. Park, Y. Lin, Y. Tian, Y.H. Hu, X. Li, Y. Kamimoto, R. Ichino, Facile hydrothermal synthesis of **EAB**-type zeolite under static synthesis conditions. Cryst Res Technol. 56, 2000163.

[29] L. Olsson, K. Wijayanti, K. Leistner, A. Kumar, S.Y. Joshi, K. Kamasamudram, N.W. Currier, A. Yezerets, 2016. A kinetic model for sulfur poisoning and regeneration of Cu/SSZ-13 used for NH_3-SCR. Appl Catal B-Environ. 183, 394-406.

[30] Y. Jangjou, Q. Do, Y. Gu, L.-G. Lim, H. Sun, D. Wang, A. Kumar, J. Li, L.C. Grabow, W.S. Epling, 2018. Nature of Cu active centers in Cu-SSZ-13 and their responses to SO_2 exposure. ACS Catal. 8, 1325-1337.

[31] F. Gao, J. Szanyi, 2018. On the hydrothermal stability of Cu/SSZ-13 SCR catalysts. Appl Catal A-Gen. 560, 185-194.

[32] Y. Shan, W. Shan, X. Shi, J. Du, Y. Yu, H. He, 2020. A comparative study of the activity and hydrothermal stability of Al-rich Cu-SSZ-39 and Cu-SSZ-13. Appl Catal B- Environ. 264, 118511.

[33] J. Woo, D. Bernin, H. Ahari, M. Shost, M. Zammit, L. Olsson, Understanding the mechanism of low temperature deactivation of Cu/SAPO-34 exposed to various amounts of water vapor in the NH_3-SCR reaction, Catal. Sci. Technol., 9 (2019) 3623-3636.

[34] R. Li, P. Wang, S. Ma, F. Yuan, Z. Li, Y. Zhu, 2020. Excellent selective catalytic reduction of NO_x by NH_3 over Cu/SAPO-34 with hierarchical pore structure. Chem Eng J. 379, 122376.

[35] Q. Huang, N. Chen, L. Liu, K.S. Arias, S. Iborra, X. Yi, C. Ma, W. Liang, A. Zheng, C. Zhang, J. Hu, Z. Cai, Y. Liu, J. Jiang, A. Corma, 2020. Direct synthesis of the organic and Ge free Al containing BOG zeolite (ITQ-47) and its application for transformation of biomass derived molecules. Chem Sci. 11, 12103-12108.

[36] C. Peng, R. Yan, H. Peng, Y. Mi, J. Liang, W. Liu, X. Wang, G. Song, P. Wu, F. Liu, 2020. One-pot synthesis of layered mesoporous ZSM-5 plus Cu ion-exchange: Enhanced NH_3-SCR performance on Cu-ZSM-5 with hierarchical pore structures. J Hazard Mater. 385, 121593.

[37] H. Jiang, B. Guan, X. Peng, R. Zhan, H. Lin, Z. Huang, 2020. Influence of synthesis method on catalytic properties and hydrothermal stability of Cu/SSZ-13 for NH_3-SCR reaction. Chem Eng J. 379, 122358.

[38] Z. Zhang, R. Li, M. Wang, Y. Li, Y. Tong, P. Yang, Y. Zhu, 2021. Two steps synthesis of $CeTiO_x$ oxides nanotube catalyst: Enhanced activity, resistance of SO_2 and H_2O for low temperature NH_3-SCR of NO_x. Appl Catal B-Environ. 282, 119542.

[39] L. Jiang, Q. Liu, G. Ran, M. Kong, S. Ren, J. Yang, J. Li, V_2O_5-modified Mn-Ce/AC catalyst with high SO_2 tolerance for low-temperature NH_3-SCR of NO, Chem. Eng. J., 370 (2019) 810-821.

[40] J. Du, X. Shi, Y. Shan, G. Xu, Y. Sun, Y. Wang, Y. Yu, W. Shan, H. He, Effects of SO_2 on Cu-SSZ-39 catalyst for the selective catalytic reduction of NO_x with NH_3, Catal. Sci. Technol., 10 (2020) 1256-1263.

[41] Z. Chen, C. Fan, L. Pang, S. Ming, P. Liu, T. Li, 2018. The influence of phosphorus on the catalytic properties, durability, sulfur resistance and kinetics of Cu-SSZ-13 for NO_x reduction by NH_3-SCR. Appl Catal B-Environ. 237, 116-127.

[42] J. Song, Y. Wang, E.D. Walter, N.M. Washton, D. Mei, L. Kovarik, M.H. Engelhard, S. Prodinger, Y. Wang, C.H.F. Peden, F. Gao, 2017. Toward rational design of Cu/SSZ-13 selective catalytic reduction catalysts: Implications from atomic-level understanding of hydrothermal stability. ACS Catal. 7, 8214-8227.

[43] Y. Shan, X. Shi, Z. Yan, J. Liu, Y. Yu, H. He, 2019. Deactivation of Cu-SSZ-13 in the presence of SO_2 during hydrothermal aging. Catal Today 320, 84-90.

[44] L. Ma, Y. Cheng, G. Cavataio, R.W. McCabe, L. Fu, J. Li, 2013. Characterization of commercial Cu-SSZ-13 and Cu-SAPO-34 catalysts with hydrothermal treatment for NH_3-SCR of NO_x in diesel exhaust. Chem Eng J. 225, 323-330.

[45] R.K. Abasabadi, T.V.W. Janssens, S. Bordiga, G. Berlier, Probing the effect of the Si/Al ratio in Cu-CHA zeolite catalysts on SO_2 exposure: *in situ* DR UV-vis spectroscopy and deactivation measurements, Catal. Sci. Technol., 14 (2024) 3076-3085.

[46] R. Yu, Z. Zhao, S. Huang, W. Zhang, 2020. Cu-SSZ-13 zeolite-metal oxide hybrid catalysts with enhanced SO_2-tolerance in the NH_3-SCR of NO_x. Appl Catal B-Environ. 269, 118825.

[47] R. Xu, Z. Wang, N. Liu, C. Dai, J. Zhang, B. Chen, 2020. Understanding Zn functions on hydrothermal stability in a one-pot-synthesized Cu&Zn-SSZ-13 catalyst for NH_3 selective catalytic reduction. ACS Catal. 10, 6197-6212.

[48] J. Hun Kwak, H. Zhu, J.H. Lee, C.H.F. Peden, J. Szanyi, 2012. Two different cationic positions in Cu-SSZ-13. Chem Commun. 48, 4758-4760.

[49] S. Han, Q. Ye, S. Cheng, T. Kang, H. Dai, Effect of the hydrothermal aging temperature and Cu/Al ratio on the hydrothermal stability of Cu-SSZ-13 catalysts for NH_3-SCR, Catal. Sci. Technol., 7 (2017) 703-717.

[50] F. Gao, Y. Zheng, R.K. Kukkadapu, Y. Wang, E.D. Walter, B. Schwenzer, J. Szanyi, C.H.F. Peden, Iron Loading Effects in Fe/SSZ-13 NH_3-SCR Catalysts: Nature of the Fe ions and Structure–Function Relationships, ACS Catal., 6 (2016) 2939-2954.

[51] S. Ma, X. Zhao, Y. Li, T. Zhang, F. Yuan, X. Niu, Y. Zhu, Effect of W on the acidity and redox performance of the Cu0.02Fe0.2W TiOx (a = 0.01, 0.02, 0.03) catalysts for NH_3-SCR of NO, Appl. Catal. B: Environ, 248 (2019) 226-238.

[52] D. Wang, L. Zhang, K. Kamasamudram, W.S. Epling, *In Situ*-DRIFTS Study of Selective Catalytic Reduction of NO_x by NH_3 over Cu-Exchanged SAPO-34, ACS Catal., 3 (2013) 871-881.

[53] L. Ma, Y. Cheng, G. Cavataio, R.W. McCabe, L. Fu, J. Li, In situ DRIFTS and temperature-programmed technology study on NH_3-SCR of NO_x over Cu-SSZ-13 and Cu-SAPO-34 catalysts, Appl. Catal. B: Environ, 156-157 (2014) 428-437.

[54] S. Deng, T. Meng, B. Xu, F. Gao, Y. Ding, L. Yu, Y. Fan, Advanced MnO_x/TiO_2 Catalyst with Preferentially Exposed Anatase {001} Facet for Low-Temperature SCR of NO, ACS Catal., 6 (2016) 5807-5815.

[55] L. Zhang, L. Li, Y. Cao, X. Yao, C. Ge, F. Gao, Y. Deng, C. Tang, L. Dong, Getting insight into the influence of SO_2 on TiO_2/CeO_2 for the selective catalytic reduction of NO by NH_3, Appl. Catal. B: Environ, 165 (2015) 589-598.

[56] C. Sedlmair, B. Gil, K. Seshan, A. Jentys, J.A. Lercher, An *in situ* IR study of the NOx adsorption/reduction mechanism on modified Y zeolites, Phys. Chem. Chem. Phys., 5 (2003) 1897-1905.

[57] J. Szanyi, J.H. Kwak, R.A. Moline, C.H.F. Peden, The adsorption of NO_2 and the $NO+O_2$ reaction on Na-Y, FAU: an in situ FTIR investigation, Phys. Chem. Chem. Phys., 5 (2003) 4045-4051.

[58] Z. Zhang, L. Chen, Z. Li, P. Li, F. Yuan, X. Niu, Y. Zhu, 2016. Activity and SO_2 resistance of amorphous Ce_aTiO_x catalysts for the selective catalytic reduction of NO with NH_3: *in situ* DRIFT studies. Catal Sci Technol. 6, 7151-7162.

[59] F. Liu, H. He, Y. Ding, C. Zhang, 2009. Effect of manganese substitution on the structure and activity of iron titanate catalyst for the selective catalytic reduction of NO with NH_3. Appl Catal B-Environ. 93, 194-204.

[60] H. Jiang, B. Guan, H. Lin, Z. Huang, 2019. Cu/SSZ-13 zeolites prepared by in situ hydrothermal synthesis method as NH_3-SCR catalysts: influence of the Si/Al ratio on the activity and hydrothermal properties. Fuel. 255, 115587.

[61] J. Luo, D. Wang, A. Kumar, J. Li, K. Kamasamudram, N. Currier, A. Yezerets, 2016. Identification of two types of Cu sites in Cu/SSZ-13 and their unique responses to hydrothermal aging and sulfur poisoning. Catal Today 267, 3-9.

[62] S. Amanatidis, L. Ntziachristos, B. Giechaskiel, A. Bergmann, Z. Samaras, 2014. Impact of selective catalytic reduction on exhaust particle formation over excess ammonia events. Environ Sci Technol. 48, 11527-11534.

[63] C. Paolucci, A.A. Parekh, I. Khurana, J.R. Di Iorio, H. Li, J.D. Albarracin Caballero, A.J. Shih, T. Anggara, W.N. Delgass, J.T. Miller, F.H. Ribeiro, R. Gounder, W.F. Schneider, 2016. Catalysis in a cage: Condition-dependent speciation and dynamics of exchanged Cu cations in SSZ-13 zeolites. J Am Chem Soc. 138, 6028-6048.

[64] E. Borfecchia, P. Beato, S. Svelle, U. Olsbye, C. Lamberti, S. Bordiga, 2018. Cu-CHA-a model system for applied selective redox catalysis. Chem Soc Rev. 47, 8097-8133.

[65] E. Borfecchia, K.A. Lomachenko, F. Giordanino, H. Falsig, P. Beato, A.V. Soldatov, S. Bordiga, C. Lamberti, 2015. Revisiting the nature of Cu sites in the activated Cu-SSZ-13 catalyst for SCR reaction. Chem Sci. 6, 548-563.

925

926 Table 1 **EAB** zeolite synthesis in the 10Si: *x* Al: *y* NaOH: 5.0OSDA: 80H_2O with different Si source.

Si source	Al source	Alkali	Composition		Product		
			X	*y*	T=80 ºC (7 d)	T=100 ºC (4 d)	T=150 ºC (2 d)
TEOS	$NaAlO_2$	NaOH	0.4	3.0	Amorphous	Amorphous	Amorphous
TEOS	$NaAlO_2$	NaOH	0.6	4.0	Amorphous	Amorphous	**SOD**
TEOS	$NaAlO_2$	NaOH	0.9	5.0	Amorphous	Amorphous	**SOD**
TEOS	$NaAlO_2$	NaOH	1.2	6.0	Amorphous	**EAB**+**SOD**	**SOD**
TEOS	$NaAlO_2$	NaOH	1.3	7.0	**EAB**+**FAU**	**EAB**+**SOD**	**SOD**
TEOS	$NaAlO_2$	NaOH	1.5	8.0	**EAB**+**FAU**	**EAB**+**SOD**	**SOD**
TEOS	$NaAlO_2$	NaOH	1.7	10.0	**EAB**+**FAU**	**EAB**+**SOD**	**SOD**
fumed SiO_2	$NaAlO_2$	NaOH	0.7	3.0	Amorphous	Amorphous	**SOD**
fumed SiO_2	$NaAlO_2$	NaOH	0.8	4.0	Amorphous	Amorphous	**SOD**
fumed SiO_2	$NaAlO_2$	NaOH	0.9	5.0	Amorphous	Amorphous	**SOD**
fumed SiO_2	$NaAlO_2$	NaOH	1.1	6.0	**EAB**	**EAB**	**SOD**
fumed SiO_2	$NaAlO_2$	NaOH	1.3	7.0	**EAB**	**EAB**	**SOD**
fumed SiO_2	$NaAlO_2$	NaOH	1.5	8.0	**EAB**	**EAB**	**SOD**
fumed SiO2	$NaAlO_2$	NaOH	1.7	10.0	**FAU**	**FAU**	**SOD**

927

928

929 Table 2 Physiochemical properties of **EAB** and **Cu$_x$-EAB** catalysts.

Catalysts	Concentration content (%) [a]				S_{BET} [c] (m^2 g^{-1})	Pore Volume [b] (cm^3 g^{-1})	*Ea* (KJ/mol)	Acid amount
	SiO_2	Al_2O_3	Si/Al_{ICP}	Cu/Al				
EAB	8.3	3.6	4.6	-	196	0.20	-	3.33
Cu$_{1.06}$-EAB	8.1	3.5	4.6	0.06	186	0.20	107.9	3.89
Cu$_{2.06}$-EAB	8.4	3.6	4.7	0.12	184	0.20	86.9	3.92
Cu$_{2.53}$-EAB	8.3	3.5	4.7	0.15	176	0.20	55.2	4.01
Cu$_{2.53}$-EAB(SO_2)	8.3	3.4	4.9	0.13	164	0.20	66.7	3.02
Cu$_{3.06}$-EAB	8.2	3.6	4.6	0.19	69	0.09	55.1	1.77
Cu$_{2.61}$-CHA	10.7	3.8	5.3	0.17	572	0.20	-	3.98
Cu$_{2.61}$-CHA(SO_2)	9.7	3.4	5.7	0.16	488	0.18	-	3.12

930 [a] the component content was determined by the ICP analysis.

931 [b] derived from N_2 adsorption isotherms.

Figures Captions

Fig. 1. The NO_x conversion (A) and N_2 selectivity (B) as a function of temperature in NH_3-SCR reaction over all of the catalysts (The feed contains 500 ppm NH_3, 500 ppm NO, 5 vol.% O_2, 5 vol.% H_2O and balanced with N_2 at GHSV of 200, 000 h^{-1}); Arrhenius plots of the SCR reaction rates (C) over **$Cu_{2.53}$-EAB** catalysts (The feed contains 500 ppm NH_3, 500 ppm NO, 5 vol.% O_2, 5 vol.% H_2O and balanced with N_2 at GHSV of 400, 000 h^{-1} in the temperature range 150 – 210 ◦C); The effect of introducing 100 ppm SO_2 at 400 °C for 50 h (D) over **$Cu_{2.53}$-EAB** catalysts (The feed contains 500 ppm NH_3, 500 ppm NO, 5 vol.% O_2, 5 vol.% H_2O and balanced with N_2 at GHSV of 200, 000 h^{-1}).

Fig.2. The PXRD patterns (A and B), ^{27}Al MAS NMR patterns (C and D) , N_2 adsorption-desorption isotherms (E) and pore size distributions (F) of zeolites and their associated catalysts.

Fig.3. The NH_3-TPD curves (A nad C) and the corresponding peak areas (B and D) of zeolites and associated catalysts.

Fig.4. The SO_2-TPD curves (A nad B) of zeolites and associated catalysts.

Fig.5. The EPR profiles (A and C), H_2-TPR profiles (B and D), *in situ* DRIFTS (E) and XPS (F) spectra of all the catalysts.

Fig.6. *In situ* DRIFTS spectra of NH_3 (A), NO + O_2 (B), reaction between NO_x and adsorbed NH_3 (C), reaction between NH_3 and adsorbed NO_x (D) on adsorption on fresh and aged catalysts. Experimental conditions: sample exposed to 500 ppm NH_3, 5% O_2, N_2 as balance gas (A); 500 ppm NO, 5% O_2, N_2 as balance gas (B); 500 ppm NO, 500 ppm NH_3, 5% O_2, N_2 as balance gas (C); 500 ppm NO, 500 ppm NH_3, 5% O_2 and N_2 as balance gas (D).

Fig.7. K-edge XANES of Cu foil, Cu_2O, CuO, Cu_2SO_4, **$Cu_{2.53}$-EAB**, **$Cu_{2.53}$-EAB(SO_2)**, **$Cu_{2.53}$-EAB-used**, **$Cu_{2.61}$-CHA and $Cu_{2.61}$-CHA(SO_2)** catalysts.

Fig.8. Experimental and fitted EXAFS spectra of **$Cu_{2.53}$-EAB**, **$Cu_{2.53}$-EAB(SO_2)**, **$Cu_{2.53}$-EAB-used**, **$Cu_{2.61}$-CHA and $Cu_{2.61}$-CHA(SO_2)** catalysts.

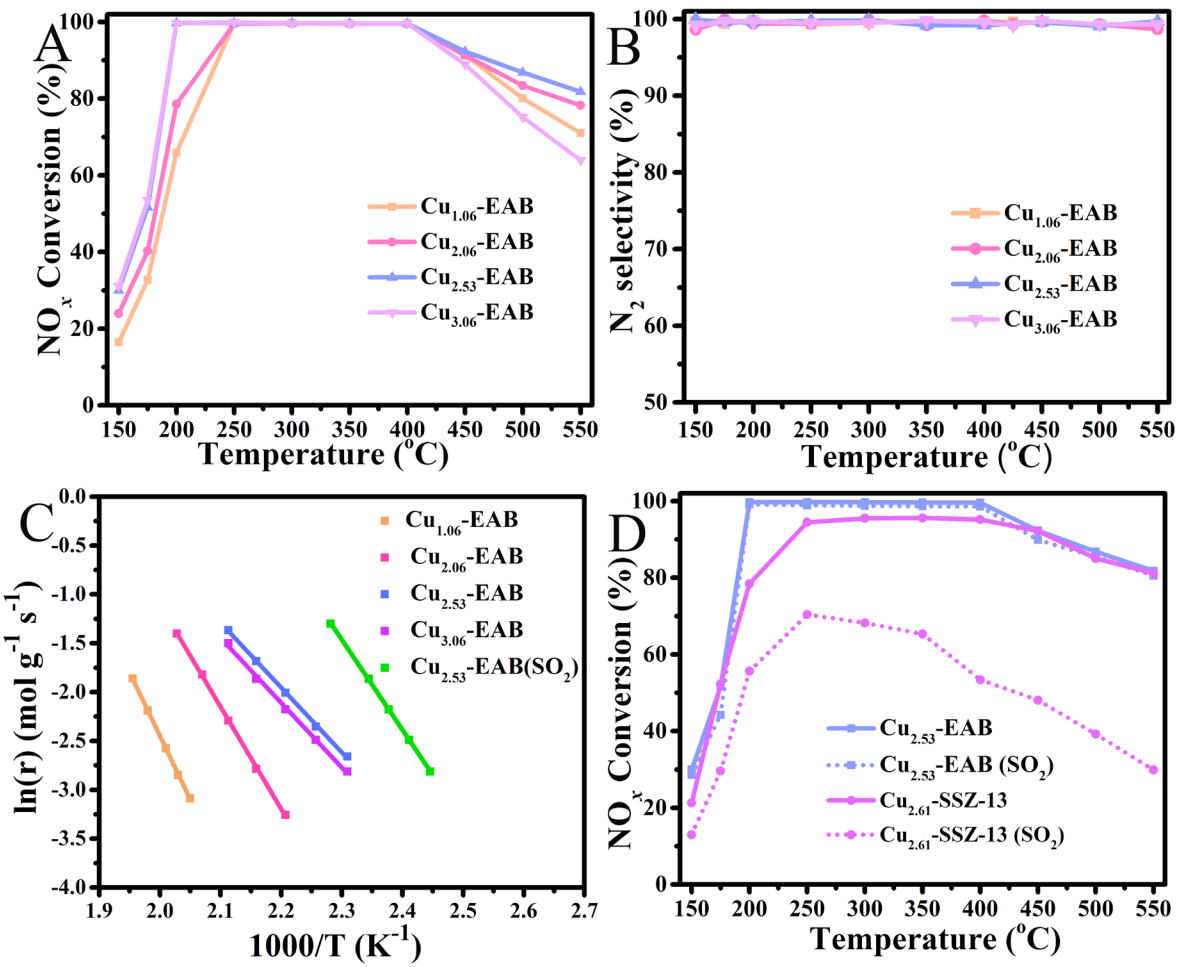

Fig.1. The NO_x conversion (A) and N_2 selectivity (B) as a function of temperature in NH_3-SCR reaction over all of the catalysts (The feed contains 500 ppm NH_3, 500 ppm NO, 5 vol.% O_2, 5 vol.% H_2O and balanced with N_2 at GHSV of 200, 000 h^{-1}); Arrhenius plots of the SCR reaction rates (C) over **Cu$_x$-EAB** catalysts (The feed contains 500 ppm NH_3, 500 ppm NO, 5 vol.% O_2, 5 vol.% H_2O and balanced with N_2 at GHSV of 400, 000 h^{-1} in the temperature range 150 to 210 °C); The effect of introducing 100 ppm SO_2 at 400 °C for 50 h (D) over **Cu$_{2.53}$-EAB**, **Cu$_{2.61}$-CHA** and their Sulfur-poisoned catalysts (The feed contains 500 ppm NH_3, 500 ppm NO, 5 vol.% O_2, 5 vol.% H_2O, 100 ppm SO_2 and balanced with N_2 at GHSV of 200, 000 h^{-1}).

967

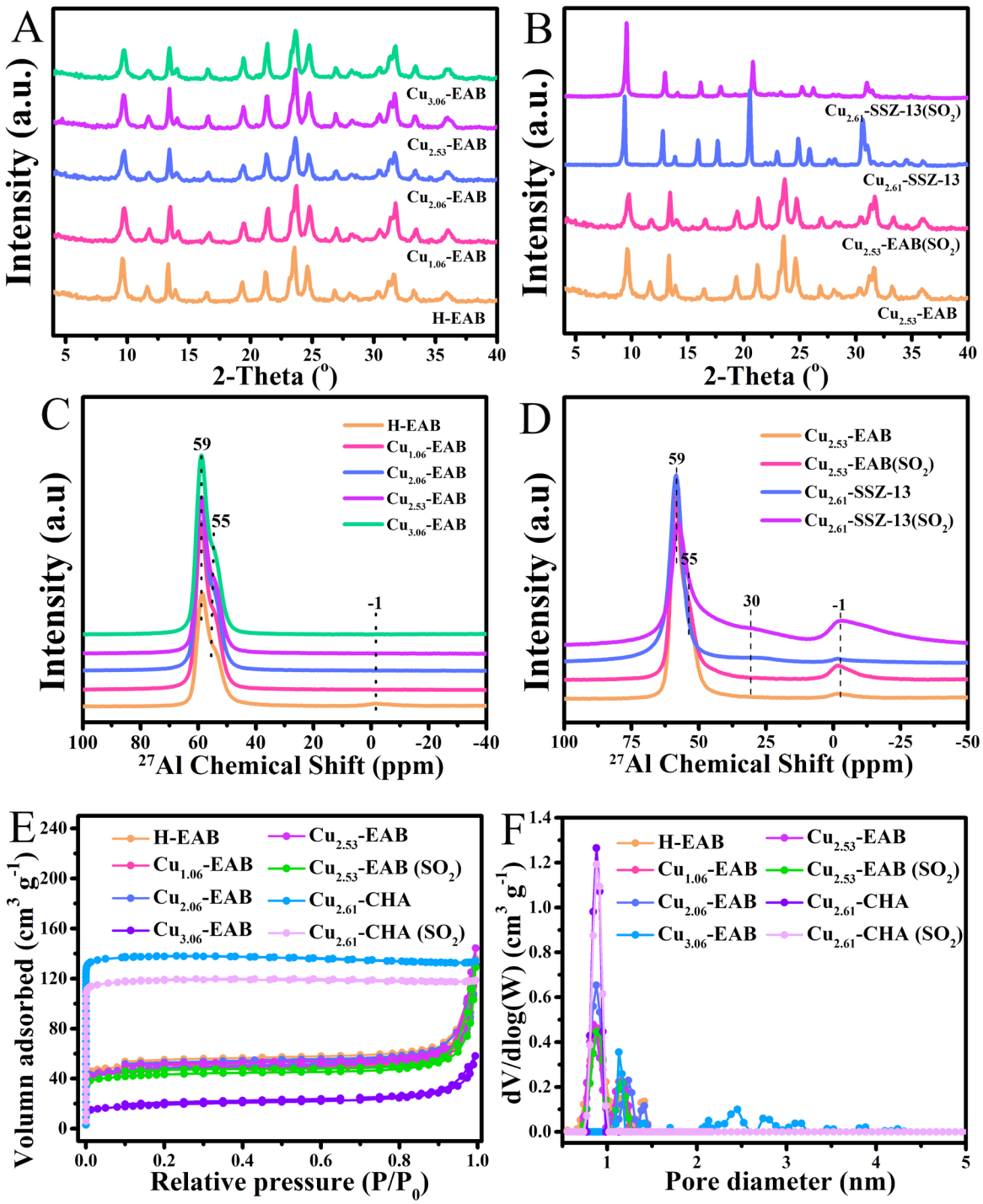

968

969 Fig.2. The PXRD patterns (A and B), ^{27}Al MAS NMR patterns (C and D), N_2 adsorption-
970 desorption isotherms (E) and pore size distributions (F) of zeolites and their associated catalysts.

971

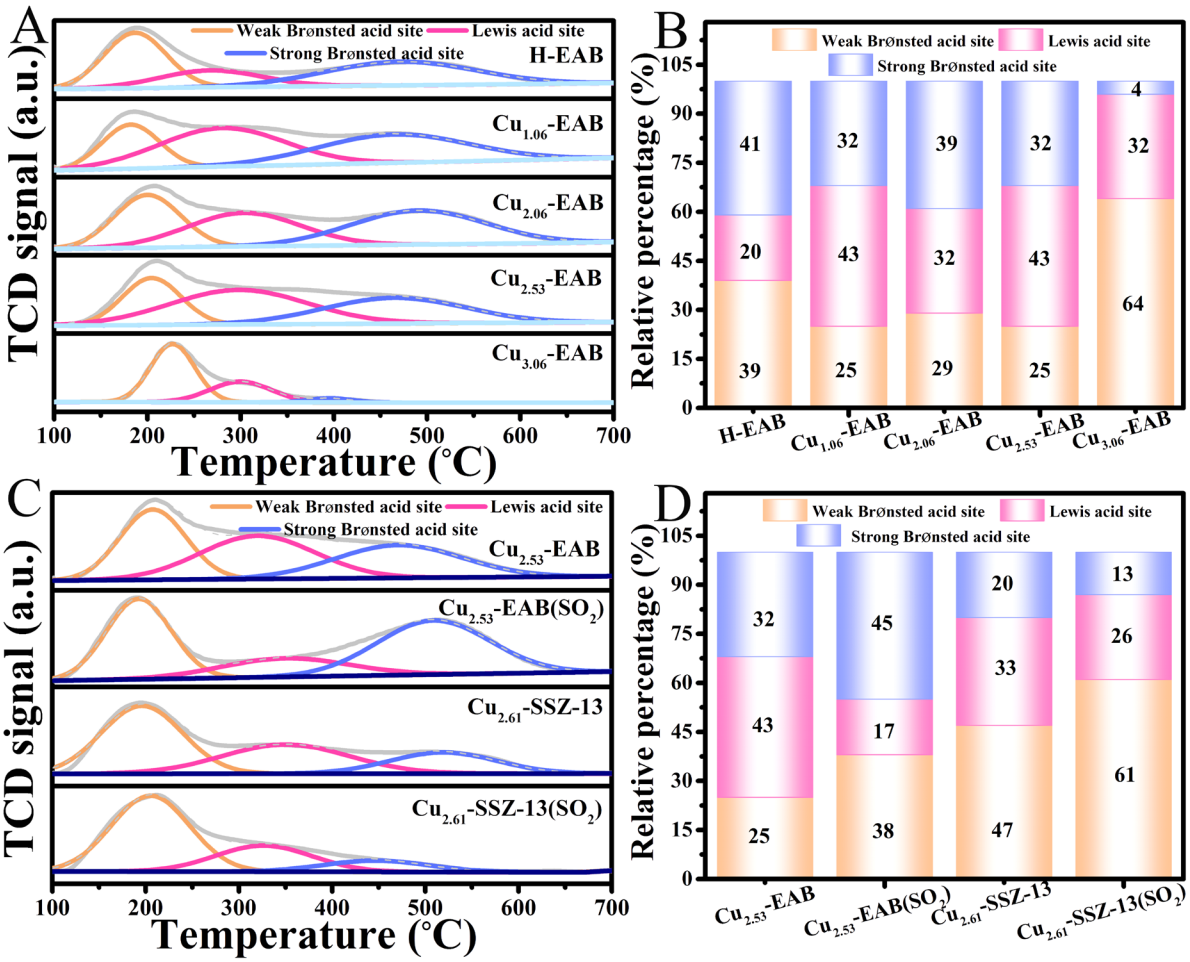

Fig.3. The NH_3-TPD curves (A nad C) and the corresponding peak areas (B and D) of zeolites and associated catalysts.

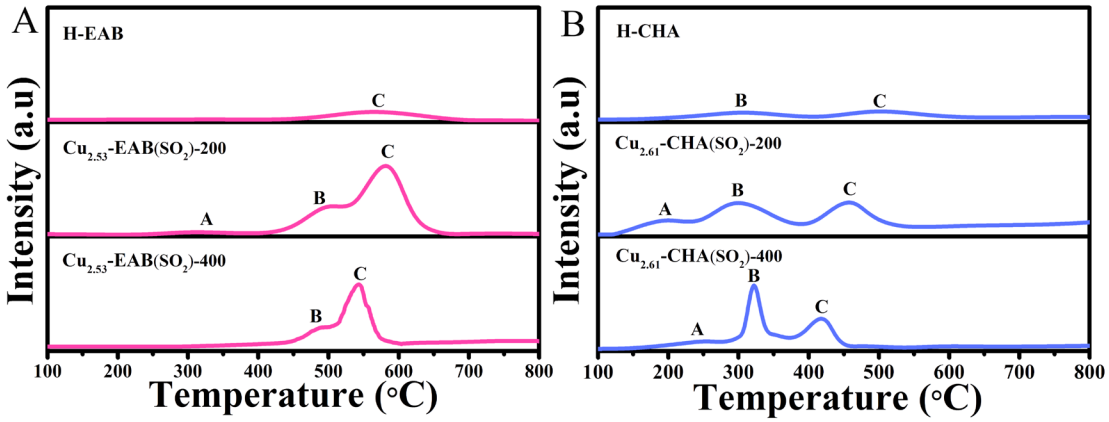

975

976 Fig.4. The SO_2-TPD curves (A nad B) of zeolites and associated catalysts.

977

978

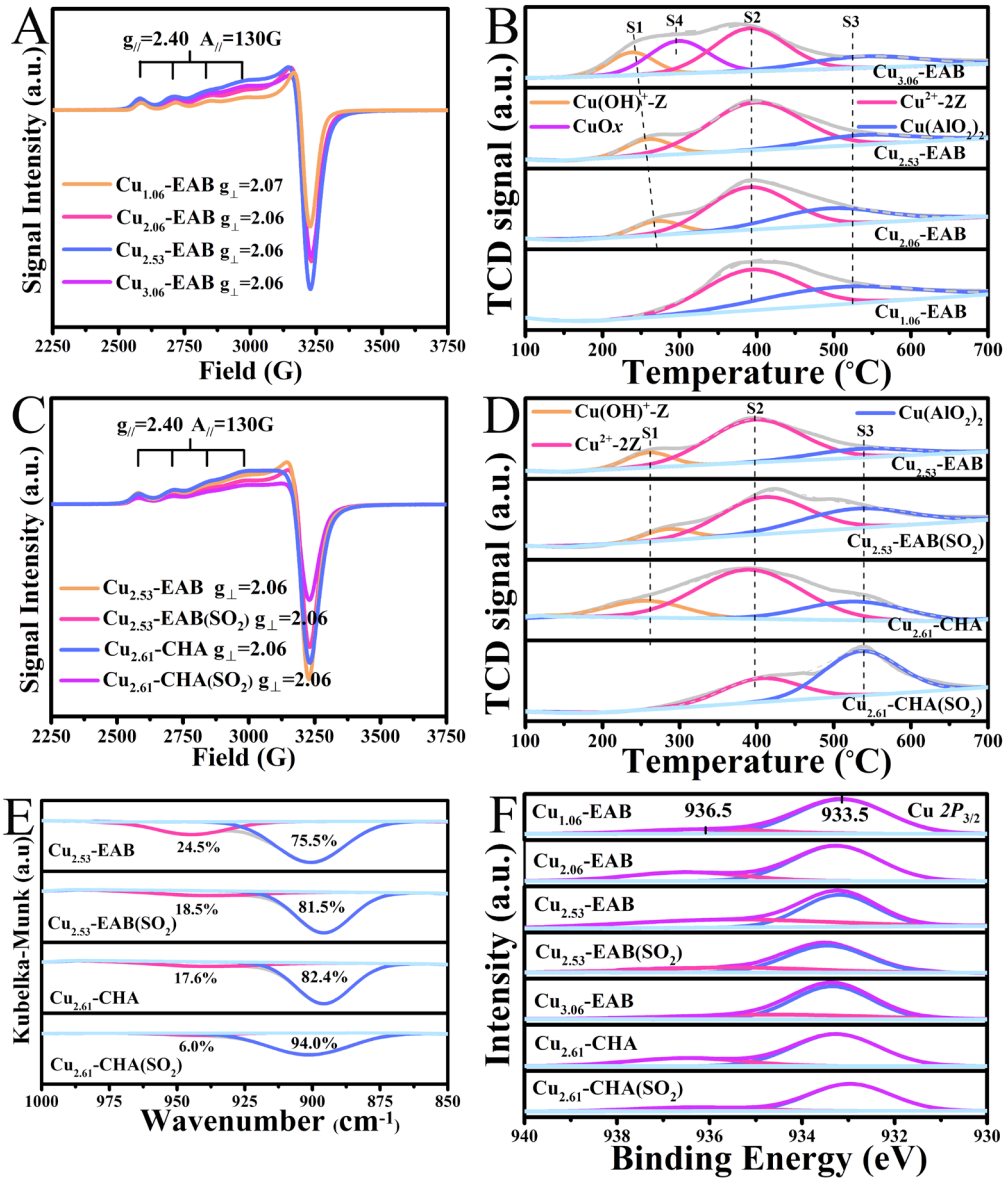

Fig.5. The EPR profiles (A and C), H_2-TPR profiles (B and D), *in situ* DRIFTS (E) and XPS (F) spectra of all the catalysts.

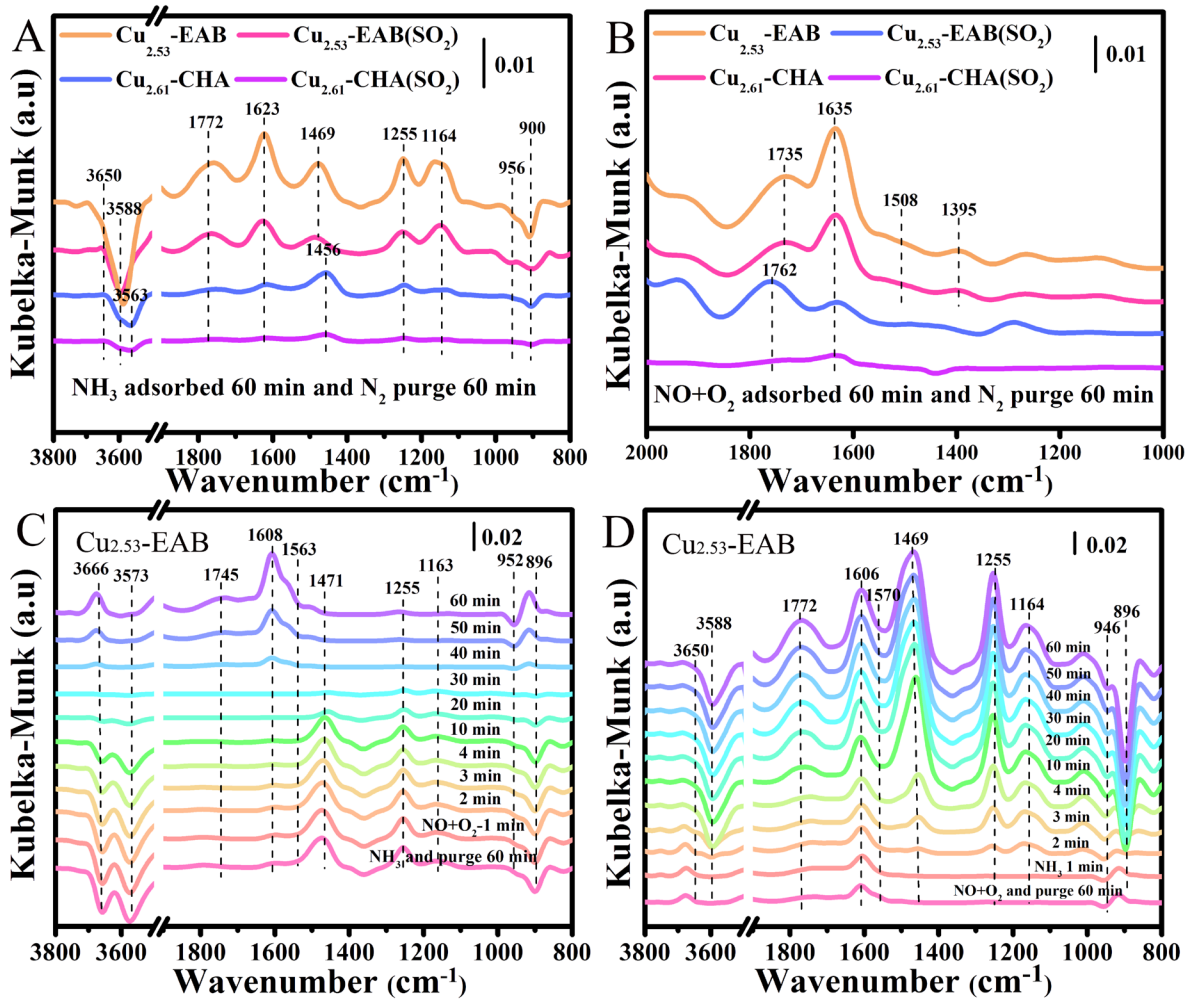

Fig.6. *In situ* DRIFTS spectra of NH_3 (A), NO + O_2 (B), reaction between NO_x and adsorbed NH_3 (C), reaction between NH_3 and adsorbed NO_x (D) on adsorption on fresh and aged catalysts. Experimental conditions: sample exposed to 500 ppm NH_3, 5% O_2, N_2 as balance gas (A); 500 ppm NO, 5% O_2, N_2 as balance gas (B); 500 ppm NO, 500 ppm NH_3, 5% O_2, N_2 as balance gas (C); 500 ppm NO, 500 ppm NH_3, 5% O_2 and N_2 as balance gas (D).

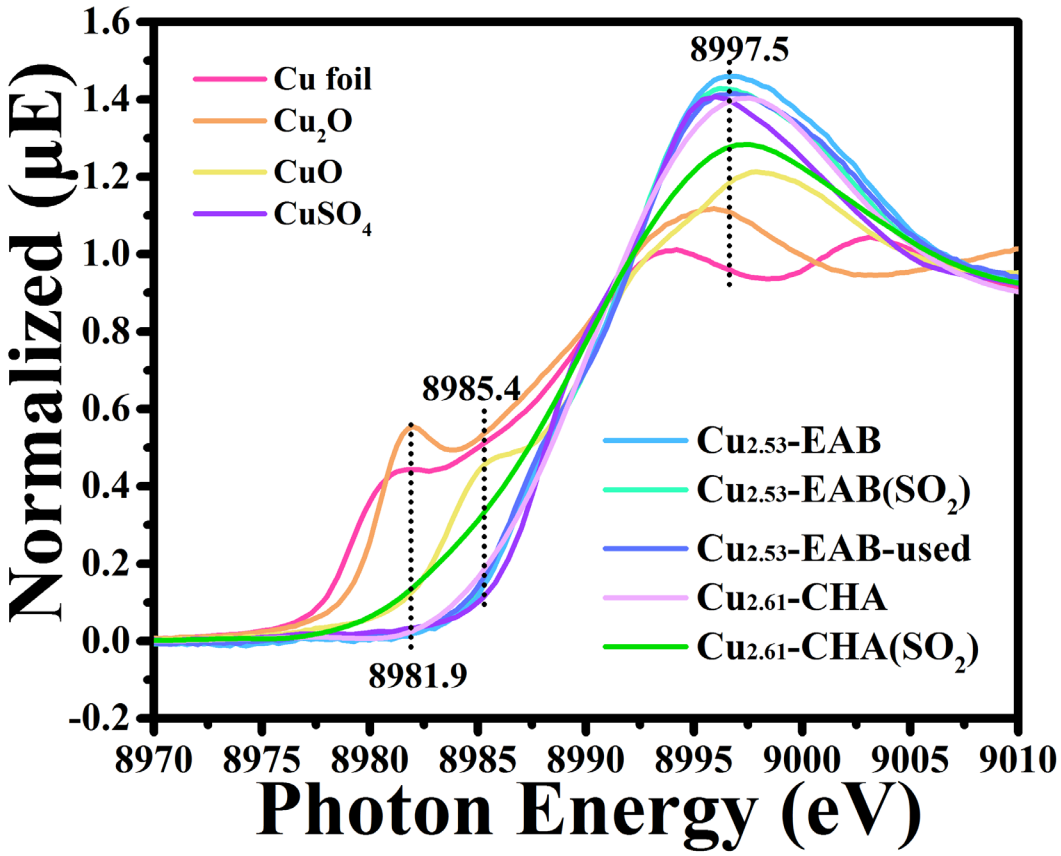

990

991 Fig.7. K-edge XANES of Cu foil, Cu_2O, CuO, Cu_2SO_4, **$Cu_{2.53}$-EAB**, **$Cu_{2.53}$-EAB(SO_2)**, **$Cu_{2.53}$-**

992 **EAB-used**, **$Cu_{2.61}$-CHA and $Cu_{2.61}$-CHA(SO_2)** catalysts.

993

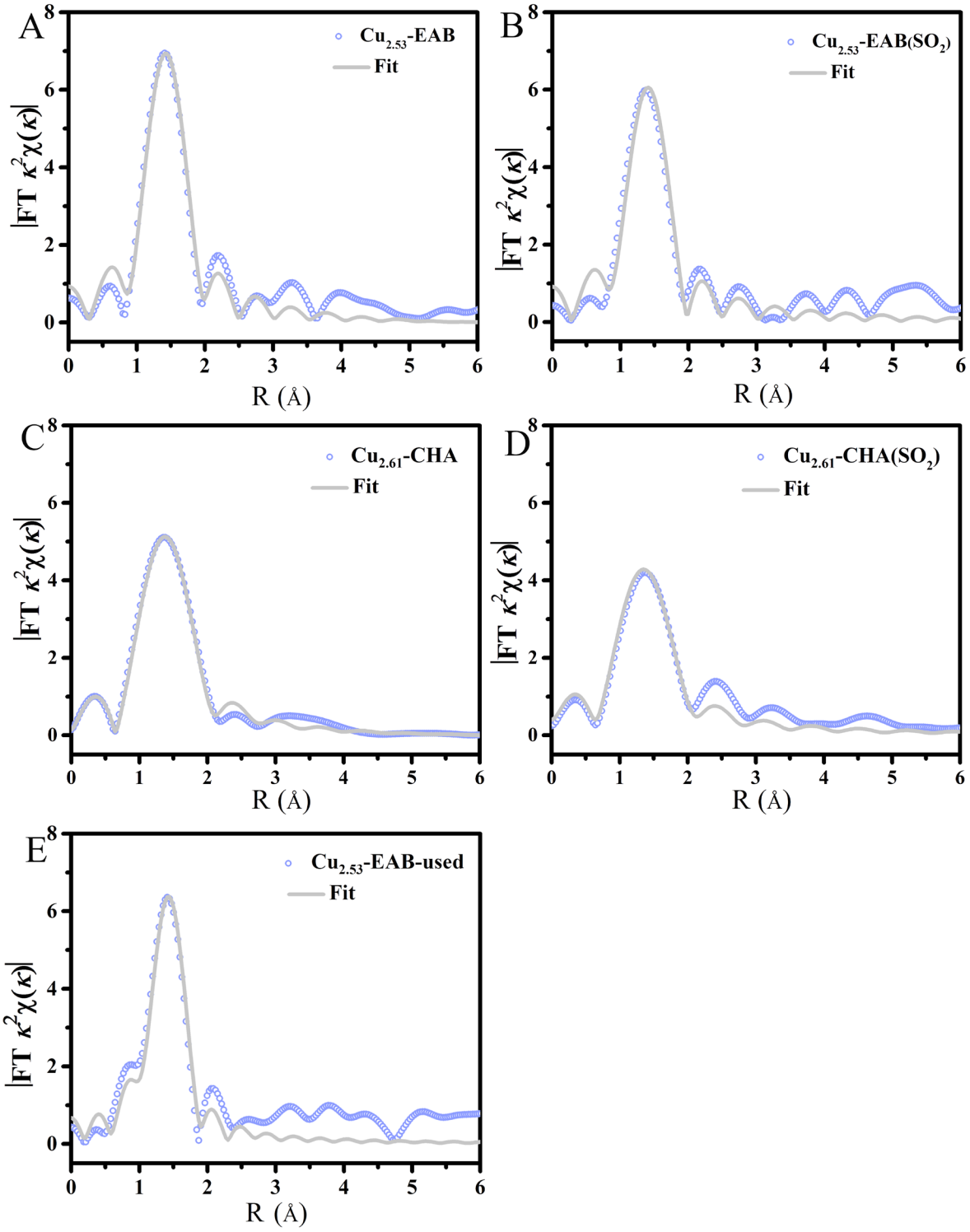

994

995 Fig.8. Experimental and fitted EXAFS spectra of **Cu2.53-EAB**, **Cu2.53-EAB(SO2)**, **Cu2.53-EAB-**

996 **used**, **Cu2.61-CHA and Cu2.61-CHA(SO2)** catalysts.